Critical Currents and Pinning Forces in $Y_1Ba_2Cu_3O_{7-\delta}$ Hi-T_c Superconductor

by

Maher Mahmoud Hussein AbdelHadi

A Thesis Presented to the

FACULTY OF THE COLLEGE OF GRADUATE STUDIES

KING FAHD UNIVERSITY OF PETROLEUM & MINERALS

DHAHRAN, SAUDI ARABIA

In Partial Fulfillment of the
Requirements for the Degree of

MASTER OF SCIENCE

In

PHYSICS

January, 1993

Order Number 1354105

Critical currents and pinning forces in $Y_1Ba_2Cu_3O_{7-\delta}$ Hi-T_c superconductor

Abdelhadi, Maher Mahmoud Hussein, M.S.

King Fahd University of Petroleum and Minerals (Saudi Arabia), 1993

U·M·I
300 N. Zeeb Rd.
Ann Arbor, MI 48106

CRITICAL CURRENTS AND PINNING FORCES IN $Y_1Ba_2Cu_3O_{7-\delta}$ Hi-T_c SUPERCONDUCTOR

BY

MAHER MAHMOUD HUSSEIN ABDELHADI

A Thesis Presented to the

FACULTY OF THE COLLEGE OF GRADUATE STUDIES

KING FAHD UNIVERSITY OF PETROLEUM & MINERALS

DHAHRAN, SAUDI ARABIA

In Partial Fulfillment of the
Requirements for the Degree of

MASTER OF SCIENCE

In

PHYSICS

JANUARY 1993

KING FAHD UNIVERSITY OF PETROLEUM AND MINERALS

DHAHRAN 31261, SAUDI ARABIA

COLLEGE OF GRADUATE STUDIES

This thesis, written by MAHER MAHMOUD HUSSEIN ABDELHADI under the direction of his Thesis Advisor and approved by his Thesis Committee, has been presented to and accepted by the Dean of the College of Graduate Studies, in partial fulfillment of the requirements for the degree of MASTER OF SCIENCE.

Thesis Committee

Thesis Advisor (Dr. K. A. Ziq)

Member (Prof. O. B. Dabbousi)

Member (Prof. G. K. Khattak)

Member (Dr. A. Hallak)

Member (Dr. H. Bahlouli)

Department Chairman

Dean, College of Graduate Studies

Feb. 6th, 1993

Date

"In the name of Allah Most Gracious,
Most Merciful"

To my Parents,
Brothers, and Sisters
with Love and Gratitude

To the Palestinian Deportees in south Lebanon,
with my hope to be allowed <u>Home</u> very soon,
God bless you

ACKNOWLEDGEMENT

First praise to ALLAH, the Almighty, who gave me strength, patience and ability to accomplish this work.

Acknowledgement is due to King Fahd University of Petroleum and Minerals for support of this research.

I would like to express my profound sense of gratitude and appreciation towards my major thesis advisor, Dr. **Khalil A. Ziq** for his continuous encouragement, moral support and generosity in sharing his time and knowledge during the research work and also in the preparation of this manuscript. His kindness, understanding, endless patience and humbleness have really impressed me. Indeed it was a great pleasure for me to work under his supervision. I am also thankful to other members of my Thesis Committee; Prof. O. Dabbousi, Prof. G. Khattak, Dr. A. Hallak and Dr. H. Bahlouli for their helpful comments, valuable suggestions and continuous encouragements.

Acknowledgement is also due to the Physics Department represented by the chairman Dr. A. Al-Harthi and faculty members for offering me this excellent opportunity to accomplish this research.

I wish also to thank Mr. Q. Azam and Mr. A. Al-Qasem in the workshop of physics dept. for their assistance in building up the sample holder. Thanks to Mr. A. Al-Bashrawi and Mr. K. Gergely in the Cryogenics lab for their

cooperation in providing me with liquid Helium and liquid nitrogen.

I am also very grateful to Prof. Riazuddin, who have contributed greatly to my physics understanding in this University, through the three graduate courses that I have taken with him.

Special thanks to Mr. N. Hamdan for his great assistance in the X-Ray analysis.

Finally, I owe my family and Dr. Abdelhamid Nassar and his wife an expression of my gratitude and grateful for their encouragement and moral support during the time of preparation of this work.

Contents

List of Tables

List of Figures

خلاصة الرسالة

الإسم الكامل : ماهر محمود حسين عبد الهادي

عنوان الدراسة : التيارات الحرجة والقوى المثبتة في $Y_1Ba_2Cu_3O_7$ فائق التوصيل ذو درجة حرارة حرجة عالية.

التخصص : الفيزياء

تاريخ الشهادة : يناير ١٩٩٣م.

تم قياس التيار والجهد الكهربائي لعينات عالية المواصفات من ($Y_1Ba_2Cu_3O_7/(AgO)x$) فائق التوصيل ذو درجة حرارة حرجة عالية وذلك تحت تأثير مجال مغناطيسي ضئيل بهدف دراسة سلوك التيارات الحرجة والقوى المُثبتة ومقاومة جريان التدفق بالقُرب من الدرجة الحرجة.

أظهرت الدراسة أن إضافة أكسيد الفضة (Ag_2O) تزيد التيارات الحرجة وتقلّل مقاومة جريان التدفق. علاوةً على ذلك لوحظ أن مقاومة جريان التدفق تُظهر نهايات (حدود) صغرى عريضة على درجات حرارة منخفضة ، ثم تبدأ بالإزدياد السّريع قُرب الدرجة الحرجة. ولوحظ ايضاً أن هذه النهايات الصغرى تُصبح حادة في الحالات الناتجة عن التبريد في وجود مجال مغناطيسي (في حالة Y_{123}) ، وهذه القيم الصغرى تحدث عند مجال مغناطيسي قريب من المجال التحريكي الحراري الحرج (B_c). وأوضحت الدراسة أيضاً بالنسبه لحالات التبريد بالمجال المغناطيسي، أن القوى المثبتة تتبع سلوك قياسي (بالقرب من الدرجة الحرجة) عندما يُعبّر عنها بدلالة نسبة المجالين (B/B_{c_2}).

فضلاً على ذلك ، وجد أن معامل اللزوجة المستخرج من مقاومة جريان التدفق وأنموذج كيم ، تُظهر نهايات عظمى لتراكيز أكسيد الفضة المختلفة ، وتصبح أكثر حدة مع زيادة التركيز. أثبتت الدراسة أن معامل اللزوجة كدالّة مع درجة الحرارة يصنع نهايات عظمى عريضة عند درجات حرارة منخفضة ويتناقص بسرعة بالقُرب من الدرجة الحرجة.

درجة الماجستير في العلوم

جامعة الملك فهد للبترول والمعادن

الظهران، المملكة العربية السعودية

يناير ١٩٩٣م

ABSTRACT

NAME : MAHER MAHMOUD HUSSEIN ABDELHADI

TITLE : CRITICAL CURRENTS AND PINNING FORCES IN $Y_1Ba_2Cu_3O_{7-\delta}$ Hi-T_c SUPERCONDUCTOR

MAJOR : PHYSICS

DATE : JANUARY 1993

Current-Voltage measurements in the presence of a small magnetic field have been preformed on high quality samples of Y_{123} and $Y_{123}/(Ag_2O)_x$ Hi-T_c superconductors, to study the behaviour of the critical currents, pinning forces and flux flow resistance (FFR) near T_c.

The addition of Ag_2O enhances the critical currents and reduces the flux flow resistance in all flux flow regions. Moreover FFR exhibits a broad minimum at low temperatures, then diverges near T_c. This minimum becomes sharper in the field cooled states of Y_{123}, and occurs at fields near B_c. The field cooled pinning forces follow a scaling behaviour (near T_c) as a function of the reduced field B/B_{c_2}.

Furthermore, Viscosity coefficient η, deduced from the FFR and Kim's model, displays sharp peaks for different Ag_2O concentrations x, with sharper peaks for higher x. Viscosity coefficient η versus temperature exhibits broad maximum at low temperatures and decreases rapidly close to T_c.

MASTER OF SCIENCE DEGREE
KING FAHD UNIVERSITY OF PETROLEUM AND MINERALS

Dhahran, Saudi Arabia
January 1993

Chapter 1

INTRODUCTION

A sharp and sudden drop of the resistance of elemental mercury was first observed by Kamerlingh Onnes in 1908. With that finding the field of superconductivity was born. A year later Onnes discovered that the application of a sufficiently strong magnetic field restored the resistance to its normal state [1].

In 1933, another surprizing and distinguishing characteristics of superconductivity was discovered by Meissner and Ochsenfeld [2] namely, its perfect diamagnetism. They found that when a superconductor (SC) is cooled below its transition temperature T_c in a magnetic field, the field is expelled out of the interior of the SC (i.e $B = 0$ inside). This effect is known now as Meissner-Ochsenfeld effect.

1.1 Overview

The Meissner effect stimulated the London brothers to propose their equations in 1935, which provided an explanation for the Meissner effect by predicting a kind of penetration depth λ_L characterizing how far a static external magnetic field can penetrate into a SC. They assumed that this parameter depends on the density of the superconducting electrons n_s [3].

Another important "length" parameter which plays an important role in understanding the superconducting transition is known as the coherence length, it was introduced by Pippard in 1950 [4]. Pippard proposed that the density of the superconducting electrons n_s (or the fraction of the total system which finds itself in the superconducting state) changes gradually over a certain length ξ which he called the range of coherence of the superconducting wave function. The range of coherence ξ can also be regarded as the distance over which the correlation between cooper pairs is effective. One consequence of the existence of the coherence length ξ is that the boundary between a normal and superconducting regions can not be sharply defined because the density of the superelectrons changes gradually with distance (away from the center of the vortex core, see Chapters 3 and 4) [7,5].

In 1950, Ginzburg and Landau (G-L) [6] proposed a phenomenological theory, mainly to overcome the short coming of the London theory. The basic assumption of this theory is that the behaviour of the superconducting electrons can be described by a wave function ψ (as an order parameter),

such that the density of the superconducting electrons is

$$n_s = |\psi|^2 \tag{1.1}$$

The theory assumes that the transition from normal to superconducting state in the absence of an applied magnetic field is a second order phase transition (in this phase transition both the free energy g and its first derivative with respect to the temperature $(\frac{\partial g}{\partial T})$ are continuous). Moreover the theory succeeded in describing the behaviour of SC's in strong magnetic fields.

When written in a dimensionless form, the G-L equations provide a dimensionless parameter $\kappa = \lambda/\xi$, known as G-L parameter. This parameter allows two different solutions to the G-L equations. The first with $\kappa < 1/\sqrt{2}$ and a positive surface energy associated with the domain between the normal and superconducting region in the intermediate state (applicable to type-I SC). The second solution with $\kappa > 1/\sqrt{2}$, the G-L equations yield a negative surface energy associated with the phase boundary (applicable to type-II SC) [7]. Ginzburg-Landau theory predicted the existence of Type-II SC's long time before its discovery.

In 1957 Abrikosov (landau's student) investigated the $\kappa > 1/\sqrt{2}$ ($\xi < \lambda$) solution and the negative surface energy [8]. He pointed out that there might be another class of SC's with different properties. He found that instead of a discontinuous breakdown of superconductivity at H_c for type-I SC's, there was a continuous increase in the magnetic flux penetration starting at a critical field H_{c_1} (called the lower critical field) and reaching $B = H$ at another higher critical field H_{c_2}.

Abrikosov also found out that normal regions (vortices) would occur where the magnetic field penetrates the superconducting state. Moreover the appearance of a normal region would release some energy and reduce the total free energy hence producing a more stable configuration [7].

1.2 Mixed State

As pointed out by Abrikosov (for a type-II SC), upon exceeding the lower critical field (H_{c_1}), magnetic flux starts penetrating into the sample. In order to produce minimum free energy, the material should split into a large number of normal regions distributed inside the superconducting material whose boundaries lie parallel to the applied field. The arrangement being such as to give the maximum boundary area relative to the volume of the normal regions, this arrangement would make the increase in the free energy due to the bulk of the normal region less than the decrease in the free energy to its surface, and so the net result is a negative surface energy.

It turns out that the shape of the normal regions that would allow a maximum surface to volume ratio is a sort of cylinders (normal cores) aligned parallel to the applied magnetic field. So it is expected for the normal cores to have a very small radius since the smaller the radius of the cylinder the larger the ratio of its surface area to its volume. This state is a mixed state of superconducting and normal conducting regions. Hence the names mixed state or Abrikosov state are commonly used. The existence of such a state

will allow a partial flux penetration between H_{c_1} and H_{c_2}, and reduces the diamagnetic energy that holds the field out, so H_{c_2} can be much higher than H_c and H_{c_1}. This property makes it possible to obtain strong magnetic field with negligible power losses [5].

The equilibrium of a SC in the mixed state can be understood by the following argument. Below H_{c_2} the bulk of the material is still diamagnetic, i.e. the flux due to the applied magnetic field is being opposed by a diamagnetic surface current which circulates around the perimeter of the specimen. Within each normal core (of radius = ξ, coherence length) is a magnetic flux equal to the flux quantum ϕ_0 having the same direction of the applied field. The flux within each core is produced by a vortex of persistent current that circulates around the core opposite to that of the diamagnetic surface current.

The vortex current encircling a core interacts repulsively with the magnetic field produced by neighbouring cores. As a result any two cores threading a SC in the mixed state do not lie at random but arrange themselves into a regular periodic array. This array usually known as the flux lattice lines. In fact it has been found that this array forms a triangular close packed lattice [5].

The density of the superelectrons n_s falls to zero at the center of each vortex line. However the flux density due to the applied magnetic field is a maximum at the center of the normal cores and falls to a small value over a distance equal to the penetration depth λ away from the cores, (see Fig. 1.1).

Finally as the field increases ($H \gg H_{c_1}$) the volume occupied by the

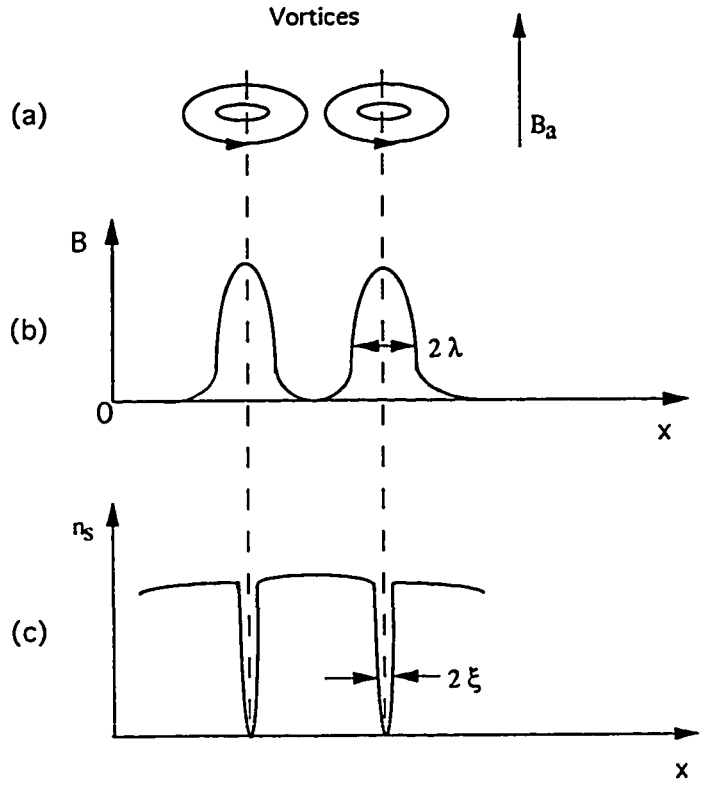

Figure 1.1: Mixed state in applied magnetic field greater than H_{c_1}. (a) Lattice of cores and associated vortices (b) variation of the flux density (c) variation with position of n_s.

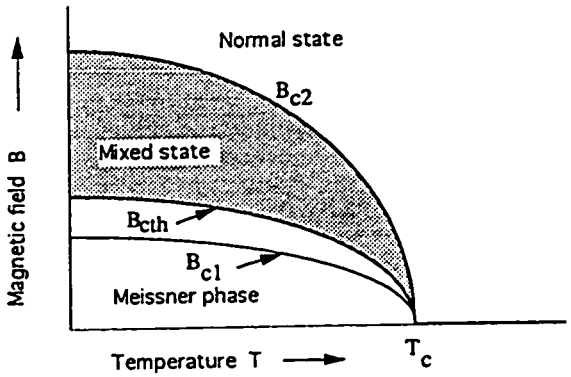

Figure 1.2: Phase diagram of a type-II SC (schematic representation).

normal regions increases, the vortex lines get closer together, and at some field strength H_{c_2} superconductivity is completely destroyed and the material becomes normal. Fig. 1.2 shows a phase diagram for the different regions [9,1].

1.3 Surface Energy

One major contribution of the G-L theory is its explanation and prediction of the intermediate state for type-I SC in which superconducting and normal regions coexist in the presence of field $H = H_c$. In order to have the two phases in equilibrium, one needs to assume a surface energy between the two

phases in the intermediate state [7].

The origin of this surface energy is very much related to the concept of coherence. If the two phases (normal and superconducting) are to be in equilibrium, their free energy per unit volume must be the same. Due to the presence of the ordered superelectrons, the free energy density of the superconducting state will be lowered by an amount $g_n - g_s$, where g_n and g_s are the free energy density in the normal and superconducting regions respectively. On the other hand the superconducting region will acquire a magnetization which cancels the flux density inside, this will result in a positive magnetic contribution ($E_M = \frac{1}{2}\mu_0 H_c^2$) to its free energy. Now since n_s rises only gradually over a distance ξ, then the decrease in the free energy due to the increasing order of the electrons takes place over the same distance (pay an energy of $\frac{1}{2}\mu_0 H_c^2 \xi$). On the other hand the magnetic energy rises over a distance of λ (gain an energy of $\frac{1}{2}\mu_0 H_c^2 \lambda$). In general ξ and λ are different, depending on SC, whether it is type-I or type-II, so the two contributions do not cancel exactly near the boundary. For type-I SC $\xi > \lambda$, there is a positive surface energy of $\frac{1}{2}\mu_0 H_c^2(\xi - \lambda)$ per unit area of the boundary, for type-II SC $\xi < \lambda$, the surface energy is negative and equals to $\frac{1}{2}\mu_0 H_c^2(\xi - \lambda)$ per unit area of the boundary [5].

1.4 Magnetic Properties

The negative magnetization for a type-I SC increases linearly with applied field and suddenly decreases to zero discontinuously at the critical field H_c, the total magnetic flux inside the SC cancels out completely [10]. In type-II SC's the magnetization exhibits similar behaviour (perfect diamagnetism) only up to a lower critical field H_{c_1}. Upon further increase of the applied field, the flux inside the material is no longer equal to zero, the average flux density in the material increases and the magnitude of the negative magnetization decreases smoothly with increasing H_a (applied field). Near the upper critical field H_{c_2} the flux density and the magnetization change linearly with field. Above H_{c_2} the material becomes normal with flux density equal to $\mu_0 H_a$ and zero magnetization [5].

From general thermodynamic considerations at constant temperature and pressure, one can find out that the area under the magnetization curve (solid line in Fig. 1.3) equals the difference between G_n and G_s (the Gibbs free energy in the normal and superconducting states respectively), we obtain

$$G_n - G_s = -\int_0^{H_{c_2}} M dH \tag{1.2}$$

For comparison purposes, consider a type-I SC that possesses the same difference in the Gibbs free energy $G_n - G_s$. Its magnetization curve is then given by the broken line (Fig. 1.3). The areas under the two magnetization curves (dashed and solid curves in Fig. 1.3) must be identical. From this requirement one obtains a relation between H_c and H_{c_2} [1].

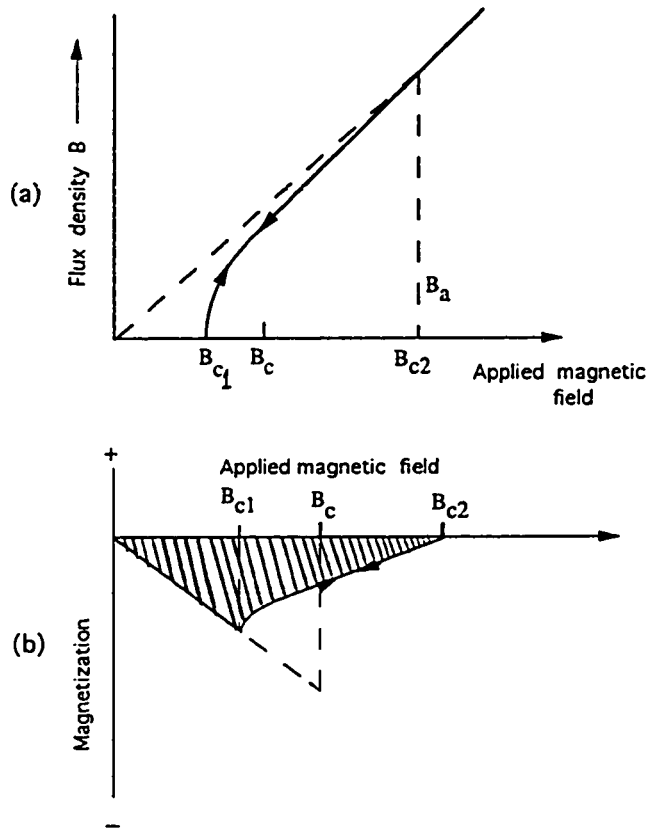

Figure 1.3: Magnetic flux density (a) and magnetization (b) versus applied magnetic field for type-II SC. The dotted right angled triangle is drawn to have an area equal to the shaded area within the magnetization curve.

1.5 Irreversibility and Pinning Forces

The magnetization curves discussed in the previous section are for an ideal type-II SC's (SC's in which the flux tubes of the mixed state are free to move and they do not have any energetically preferred positions). In this case the magnetization is reversible and do not depend on the path taken by the field whether increased from zero or decreased from some value higher than H_{c_2}. Hard SC's (sometimes known as type-III SC's), show some irreversibility in their magnetic behaviour. This irreversibility is attributed to the fact that the flux tubes, in the mixed state are attracted to defects and imperfections present in the material and get stuck or pinned there and so they are prevented from being able to move. For this reason these impurities and defects are called pinning centers, since they experience a sort of force that prevent the motion of these vortices, this force is called the pinning force [13].

To understand irreversibility in the magnetic behaviour in type-II SC's let us study the mechanism of flux lines motion. Upon increasing the magnetic field from zero there is no sudden entry of flux at H_{c_1} as in the ideal case. Above H_{c_1}, the negative magnetization gradually decreases, approaching zero as the applied field approaches H_{c_2}. The cores formed at the surface are hindered from moving into the interior. This will increase the thickness of the screening layer and therefore increases the total screening current, which in turn increases the magnetization higher than the corresponding value in the ideal case. Similarly on reducing the field from above H_{c_2}, there is a

hysteresis loss associated with increasing and decreasing field, and flux lines may be left permanently trapped in the sample. That is because some of the vortices are pinned to the defects and can not escape their pinning potentials. The effective radius of the pinning potential is roughly equal to the radius of the pinning center, hence the pinning centers are effective only when their dimension are comparable to the coherence length (ξ) which is the radius of the vortex [5].

Pinning the normal cores by imperfections plays a very important role in determining the critical currents of type-II SC's. This important subject will be discussed in the next section, (see also Chapter 4).

1.6 Critical Currents

Below a certain critical value known as I_c, the electric field inside a SC is equal to zero and therefore the SC remains resistanceless. Upon exceeding this critical value (in type-II SC) a voltage drop develops along the SC (in the direction of the current), and a resistance (known as flux flow resistance) starts to appear, and the current is distributed through the whole body of the material. The current flowing through type-I SC is only confined to pass within a surface layer of thickness equal to the penetration depth λ [5].

It is important to understand that there is a direct relation between the critical currents and the critical magnetic fields. In general there are two contributions to the current flowing within the surface of a SC. First: trans-

port current J_i which is induced by an external source. Second: screening current J_H, appears as a result of applying a magnetic field on the SC. The screening current circulates in the surface so as to cancel the flux inside the SC. At any point the total critical current density J is equal to the sum of the two contributions

$$J = J_i + J_H \tag{1.3}$$

Superconductivity will disappear if at any point the value of J exceeds an upper critical current density J_c. If the critical current density at the surface is equal to J_c then this value will be associated with a magnetic field equal to H_c at the surface. This leads to the so called Silsbee's hypothesis for type-I SC. According to this hypothesis the critical current is the maximum transport current which can be passed through a SC without resistance (i.e without energy losses). Clearly the stronger the applied magnetic field the smaller is the critical current [5,1].

The situation in type-II SC is however, more complicated because the superconducting properties of the material changes at two critical fields H_{c_1} and H_{c_2}. The behaviour of the critical currents in the mixed state plays an important role in our study, and will be discussed in more details in Chapter 4.

1.7 BCS Theory

In 1957, Bardeen,Cooper and Schrieffer proposed a basic quantum microscopic theory of superconductivity (known as BCS theory) [11]. This theory gained a universal acceptance as it has successfully explained many observed features of the superconducting state.

The central feature of the theory is that two electrons near the Fermi surface in a SC are able to form a bound state known as Cooper pair. They experience an attractive interaction strong enough to overcome their mutual electrostatic repulsion. This attraction would be obtained if the electrons interact with each other via the quantum vibration of the crystal lattice as the lattice structure is momentarily deformed by a passing electron. This passing electron pulls ions of the lattice in its vicinity, causing the region around it to contain more positive charges than before. The electron pass through and the region remains positive for a while until a second electron is attracted toward it. In other words one can say that the attractive force between the two electrons making up a Cooper pair is an electron-lattice-electron interaction, where the lattice serves as the mediator of the attractive force. Cooper pair consists of two electrons with equal and opposite momenta and spin, so it forms a system of zero total momentum and zero spin. Therefore it behaves like boson and a large number of them can be in the same quantum state [14].

As expected from any good theoretical model, the BCS theory not only explained most experimental data at that time but also predicted new phe-

nomena which were later on observed experimentally such as:

1. For most superconducting materials the energy gap E_g is proportional to the transition temperature

$$E_g \approx 3.53 K_B T_c \tag{1.4}$$

2. The transition temperature is related to Debye temperature θ_D, the electron-phonon coupling constant u and the electron density of state at Fermi level $D(\epsilon_f)$ by

$$T_c = 1.134 \theta_D \exp[-1/uD(\epsilon_f)] \tag{1.5}$$

or with the electron-phonon-electron coupling constant α

$$T_c = 1.134 \theta_D \exp[-1/\alpha] \tag{1.6}$$

3. Penetration depth, coherence length and the London equations are a consequence of the BCS theory.

4. There is a discontinuity in the electronic contribution to the specific heat at the transition temperature given by

$$\frac{C_s - C_n}{C_n} = 1.43 \tag{1.7}$$

where the subscripts s and n denote the superconducting and normal states, respectively.

5. Magnetic flux penetrating a type-II SC's is quantized with a quantum value of

$$\phi_0 = \frac{hc}{2e} \tag{1.8}$$

6. Josephson tunnelling across a tunnel junction without any voltage bias.

1.8 High-T_c Superconductivity

The highest superconducting transition temperature (T_c) for the classical type-II SC's is 23.2 K, and was achieved in 1973 for Nb_3Ge thin films. In 1986, Bednorz and Müller reported transition temperatures in 30 K range for metallic compounds of Ba-La-Cu-O system [12]. This new discovery has accelerated the search for room-temperature SC vigorously. By the end of 1986 and the beginning of 1987 other Lanthanum compounds were fabricated which raised the superconducting transition temperature (T_c) to 40 K. Shortly after that, the Y-Ba-Cu-O system was discovered with T_c's at 85-95 K [15]. In the early 1988, a new record was achieved with the discovery of the Bi-Sr-Ca-Cu-O system with $T_c \sim 110K$ [25].

Since the time of discovery of this new field of high-T_c superconductivity, a large number of scientists , researchers and engineers have got involved in the field hopping to achieve two main goals. First, to explore and understand the underlying physics behind these new SC's. Second, to develop new ceramic superconducting devices from these materials [9].

At this stage, it is interesting and helpful to review some basic common properties of this new high-T_c materials.

1. These Hi-T_c SC's are mostly copper-oxide based ceramics with transition temperature well above liquid nitrogen (LN_2) temperature.

2. The crystal structure is anisotropic showing two-dimensional features. The electrical transport properties; for example critical currents and fields, are also anisotropic with high conductivity parallel to the Cu-O planes and less conductivity perpendicular to the planes [13].

3. The electrical resistance in the normal state displays a metallic linear temperature dependence.

4. The magnetic flux is quantized as in the conventional SC's. It is believed that their superconducting state is made up of paired carriers, however the nature of this pairing force or even the type of these carriers it not really well understood.

5. The superconducting transition is accompanied by a discontinuous jump in the specific heat with $C_s > C_n$, a property which is predicted by the BCS theory as well as Gorter-Casmir theory and observed in the classical SC.

6. They are all type-II SC's with very high $\kappa = \lambda/\xi$ values (200-500). The coherence length is very small ($\xi \sim few\mathring{A}$)

7. The critical current densities are relatively small compared to the classical SC. This is due to the grain boundary, weak-link problem and to insufficient flux pinning. However, the critical field H_{c_2} is very high ($\sim 200T$ at 4.2 K for Y_{123}) [13].

1.9 Motivations and Goals

The newly discovered copper-oxide SC's are characterized by relatively low critical current densities (J_c) which significantly limit their potential technological applications. Since the discovery of these materials, several attempts have been made to increase J_c values by increasing the pinning forces. Critical current measurements in the presence of an externally applied magnetic field is a simple and powerful technique for determining the critical current density, average pinning forces and the associated flux lines dynamics.

The motion of the flux lines in the mixed state is found to be a dissipative process, or in other words it is accompanied by the electrical resistance. This resistance (known as flux flow resistance) can be easily deduced from the (I-V) curves in the different regimes of flow; flux flow, intermediate flux flow and flux jump.

It has been found experimentally that Y_{123}/Ag_2O composites affect the normal state resistance and enhances the critical current densities, since the addition of silver creates more pinning centers. However there is no detailed investigation available concerning the behaviour of the pinning forces, flux

dynamics and the associated flux flow resistance in these composites.

Motivated by these well defined problems, in such a promising field of study and motivated by the powerfulness and sensitivity of (I-V) technique, we decided to carry out this research project hopping to achieve the following goals :

1. To understand the behaviour of the critical currents and pinning forces under different experimental conditions (e.g temperature and magnetic field).

2. To understand the dynamics of the flux lattice lines in the mixed state in both Y_{123} and Y_{123}/Ag_2O systems.

3. To study the behaviour of the flux flow resistance in different regions as they reflected in the (I-V) characteristics.

4. To check the applicability of some important models like Kim's and Clem's models which were originally proposed for the classical SC's.

Chapter 2

EXPERIMENTAL TECHNIQUES

2.1 Sample Preparation

Preparation of a single phase of some Hi-T_c copper-oxide superconductors (that show a sharp transition to zero resistance and demonstrate strong magnetic levitation) is by now relatively well established methodology. In fact this is one of the reasons behind the world wide growth in studying these new ceramic SC's [16].

However, the details of preparation and sample microstructure are crucial for obtaining desirable superconducting properties, such as high critical current density (J_c) and upper critical field (H_{c_2}). High quality single phase samples require careful consideration to a number of factors such as; calci-

nation temperature and time, oxygen content, grinding procedure, grain size and final annealing temperature and time [9,16].

$YBa_2Cu_3O_{7-\delta}$ (commonly written as Y_{123}) and almost all other copper-oxide SC's can be prepared by three methods, namely, solid state reaction, coprecipitation and sol-gel techniques [16,17]. However, samples used in this study have been prepared by the solid state reaction method. This method of preparation is the easiest, yet it yields high quality single phase samples, also it is the most widely used technique for preparation of these new Hi-T_c ceramics.

2.1.1 Preparation of Y_{123}

We started by weighing out the required stoichiometric ratios (Y : Ba : Cu = 1 : 2 : 3) of high purity powders of yetterium oxide (Y_2O_3 of purity 99.9999 %), barium carbonate ($BaCO_3$, 99.99%) and copper oxide (CuO, 99.999%). The powders were mixed thoroughly and ground using an alumina mortar and pestle for about half an hour. The total mixture was placed in alumina crucible and placed in a furnace for calcination in air at 890°C for about 18 hours. During the calcination process, carbon is released from $BaCO_3$ as CO_2 and the superconducting orthorohombic phase starts to form. After fast cooling, the sample is reground for about 30 minutes and the calcination process was repeated three times. Then the resultant mixture was reground and pressed into 2-3 mm thick, 10-13 mm diameter pellets at a pressure of 3000 kg/cm^2. Finally, pellets are sintered in oxygen atmosphere

at temperature of 940°C in a tube furnace for about 20 hours. The pellets were cooled down slowly to room temperature at a rate of 5°C/min. Then the annealed pellets were reground, pelletized under the same conditions, and the annealing procedure was repeated at least one more time.

2.1.2 Preparation of $Y_{123}/(Ag_2O)_x$ Composites

The prepared pure Y_{123} samples were used to prepare $Y_{123}/(Ag_2O)_x$ composites. Appropriate weight ratio of Y_{123} powder and silver oxide (Ag_2O of purity 99%) were mixed thoroughly and ground for 30 minutes, pressed into pellets of 2mm thickness, 10-13 mm diameter under pressure of 3000 kg/cm^2. The pellets were then annealed at 950°C in oxygen atmosphere for 18 hours. The furnace was then turned off and the sample cooled slowly to room temperature at a rate of 5°C/min. This last process of annealing was repeated once more after grinding and pelletizing to ensure random distribution of the silver powder and good superconducting properties [9]. Three samples with different weight ratios were prepared, the Y_{123} to Ag_2O weight ratios are: 7:1, 10.5:1 and 14:1.

A bar-shaped samples were cut from the prepared pellets and then they were characterized as described in the following sections. The dimensions of the samples are listed in Table 2.1.

Table 2.1: **Samples Dimensions**

System	Y_{123}/Ag_2O Ratio	Length (mm)	Thickness (mm)	Width (mm)	Volume (mm^3)	Cross sectional area (mm^2)
Y_{123}	0.0	8.88	0.96	2.07	17.65	1.987
Y_{123}/Ag_2O	7:1	11.15	1.30	1.40	20.29	1.82
Y_{123}/Ag_2O	10.5:1	9.91	1.34	2.27	30.14	3.042
Y_{123}/Ag_2O	14:1	10.09	1.25	1.70	21.44	2.125

2.2 Experimental Set Up

Several parts of the experimental setup used in this project has been designed and built in the workshop of the Physics Department at KFUPM.

A block diagram of the set up is shown in Fig. 2.1. The sample holder is made of a poor thermal conductor of stainless steel rod. It is a hollow cylinder of 10 mm outer diameter and about 1 meter long. One end of the cylinder host all the electrical connections to the sample. The other end is fitted with a D-shaped copper rod which hosts a copper-constantan thermocouple embedded at its center. Copper has a very good thermal conductivity and relatively high heat capacity, thus providing a stable temperature at the sample site. The sample is placed on the flat side of the copper block just above the thermocouple junction. Samples are fixed on the holder by a

double sided tape. Electrical connections from the sample are fed through the hollow of the sample holder to the electronics. A stable current source (Keithley Model 225) is used to supply current to the sample.

The voltage is measured by Keithley, model 181 nano-Voltmeter. Thermocouple potential difference was measured using HP 3466A digital multimeter.

The sample holder was fitted to the top of a liquid helium dewar and the temperature was controlled by changing the height of the sample above liquid helium level. The reference point for our thermocouple is the liquid nitrogen temperature.

2.2.1 Magnetic Field Calibration

Most of our measurements require an application of small magnetic field (0.5 - 500 G) perpendicular to the current passing through the sample. For this purpose, our set up (shown in Figure 2.1) is provided with a small solenoid.

The wire is wound in the form of a helix with the turns closely spaced, over a teflon cylinder of 10 cm long and 10 mm inner diameter. It is designed in such a way so that it can easily slide over the copper rod of the sample holder. When placed in its proper place, the test sample lies at the center of the soleniod, since the field is most uniform and achieves its maximum value at the center of the solenoid.

In the design of this solenoid we tried to approach the case of an ideal

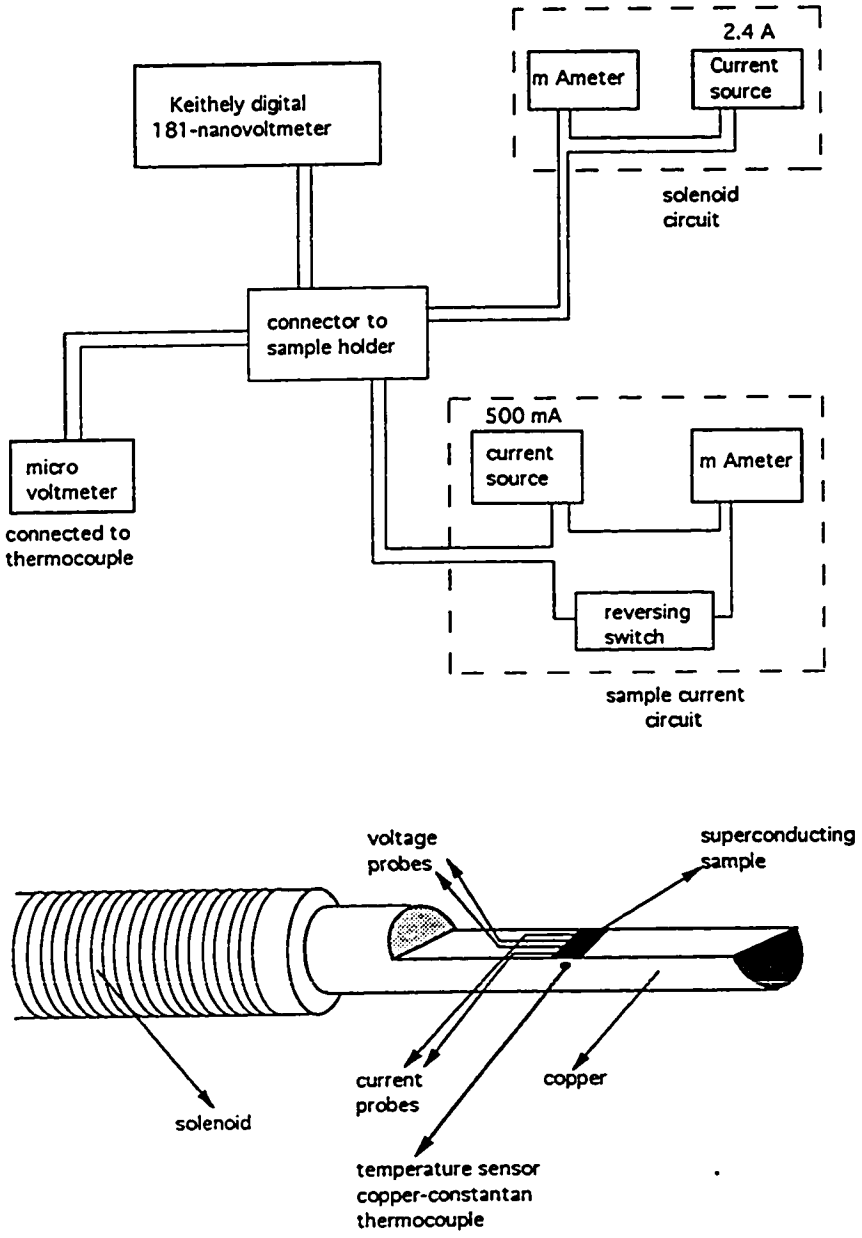

Figure 2.1: Experimental set up showing sample holder and electronics

solenoid when the turns are closely spaced and the length is long compared to its inner radius. In this case the field outside the solenoid is weak, and the field inside is uniform over a large volume.

To determine the magnetic field at any point on the axis of the solenoid one can use the Biot-Savart law to show

$$B = \frac{\mu_0 NI}{2\ell}(\sin\phi_2 - \sin\phi_1) \tag{2.1}$$

where μ_0 is the permeability of free space, N number of turns, I current passed, ℓ the length of solenoid and ϕ_1, ϕ_2 are defined in Fig. 2.2 which shows the internal geometry of the solenoid

Near the center of the solenoid the field can be approximately described by the equation

$$B = \frac{\mu_0 NI}{\ell} \qquad \phi_1 \simeq 90^\circ \text{ and } \phi_2 \simeq 90^\circ \tag{2.2}$$

However, since N is not known exactly, a calibrated Gaussmeter (Bell 620) was used to calibrate the magnetic field at the center of the solenoid and at room temperature. This calibration is also valid at low temperature. Since there is no magnetic material inside the solenoid, and μ_0 is temperature independent.

A linear fit shown in Fig. 2.3, which shows the linear changes of B versus I, was used to fit the experimental points, and yielded the following relation between B and I.

$$B = 0.18308 + (0.39382)I \tag{2.3}$$

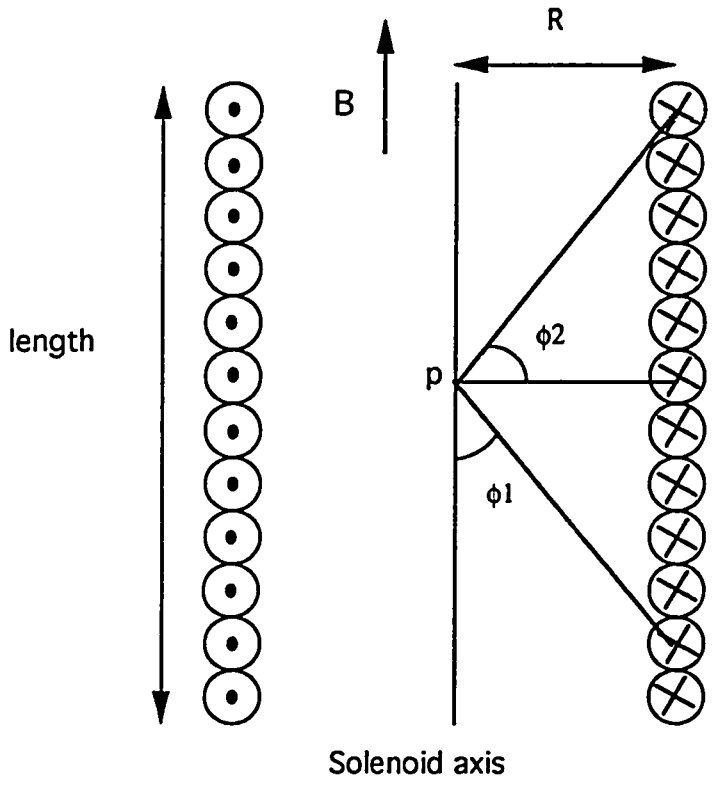

Figure 2.2: Solenoid internal geometry.

which can be used to calculate the magnitude of the applied field (in Gauss) for any passed current (in mA).

2.3 I-V Characteristics Measurements

(I-V) characteristics is the technique through which many superconducting parameters can be easily deduced such as critical current density, pinning force, flux flow resistance. The experimental procedure to carry out the measurements is as follows:

1) The sample is first cooled in the required magnetic field perpendicular to the current. This means that the field is turned on when the sample is at temperature $T > T_c$.

2) A sufficient period of time is allowed to bring the sample to the required measuring temperature.

3) A small current (I) is passed through the sample perpendicular to the field direction.

4) The corresponding induced voltage in the direction of the applied current (I) is measured for both directions of (I).

5) The current is increased in small steps, until the voltage exceeds some required value ($2 - 5\ \mu V$).

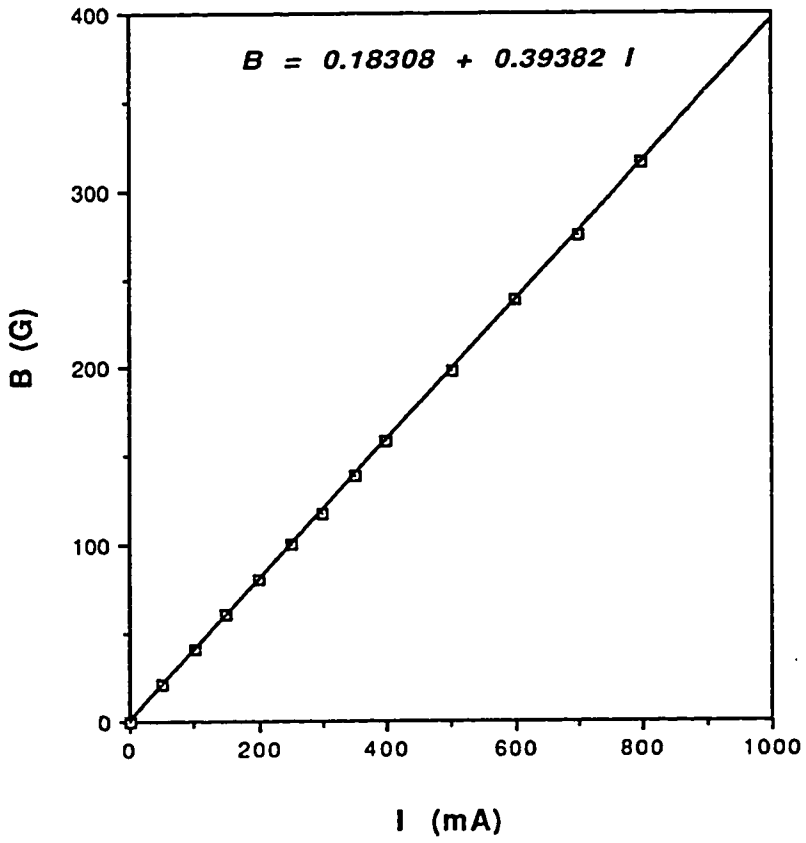

Figure 2.3: Magnetic field calibration of the solenoid.

6) V is plotted versus I, and then the (I-V) curve is used to determine different parameters that will be discussed in the coming chapters.

2.4 Sample Characterization

The commonly used methods to check the quality of the prepared samples are; the disappearance of the electrical resistance, the magnetic expulsion (Meissner effect) and x-ray diffraction for structural analysis. Magnetic expulsion is an indication about the diamagnetic properties (the ability of the sample to reject the applied magnetic field). The resistivity measurement is a good practical guide for application purposes. A sharp and high transition temperature is an indication of high quality sample.

2.4.1 Magnetic Levitation

Magnetic levitation is used as a rough quick test of the superconducting properties of the sample. For the purpose of doing that, the sample is cooled down to LN_2 (liquid nitrogen) temperature by dropping it in a cup containing LN_2. Then a small magnet is placed on the top of the sample. A small distance levitation (compared to the sample dimensions) above the sample is considered as a good rough indication about the diamagnetic properties of the sample. The levitation height (at LN_2 temp.) is proportional to the diamagnetic properties of the

sample. Typically our samples yielded 4-8 mm levitation height at LN_2 temperature.

2.4.2 Resistivity Measurements

The resistivity measurements were carried out on the bar-shaped samples. The critical temperature T_c was determined for each sample by the standard four-probe technique using silver paint to connect the probes to the samples. The sample temperature was determined by a copper-constantan thermocouple embedded in the copper block of the sample holder.

The resistance of each sample was measured over a temperature range (80-200K). For every measurement a sufficient period of time was allowed for the sample to reach thermal stability at its position. A current of 5 mA was applied to the samples during all resistivity measurements. At the equilibrium temperature, the nano-voltmeter reading for both directions of the current and the (e.m.f) of the thermocouple was recorded. It is necessary to take the reading of the nano-voltmeter for both direction of the current in order to reduce the noise and background voltage. The actual value of the sample voltage is the average of both readings. The (e.m.f) readings of the thermocouple is transferred to a temperature reading using a standard calibration table for copper-constantan thermocouple.

2.4.3 Structural Analysis

The crystallographic structure can be determined by the x-ray powder diffraction (XRD). Structural analysis reveals the presence of single or multiphase. Moreover, Lattice parameters a, b and c can be determined from (XRD) analysis.

X-Ray Diffraction

The crystal structure analysis of our samples was done using X-ray diffraction technique. XRD patterns on pieces of our samples were obtained using a computerized Phillips diffractometer Model APD 1700 at the Research Institute of KFUPM.

Copper K_α radiation of wavelength ($\lambda_\alpha = 1.54178\mathring{A}$) was used with Cu broad focus tube kept at 45 KV and 30 mA. The angle (2θ) was scanned in the range (5° - 80°) at scanning speed of 0.01°/sec.

Chapter 3

BASIC SUPERCONDUCTING PROPERTIES

3.1 Introduction

One of the most important and basic properties of a superconducting material is its transition temperature, the temperature at which the material transforms to the superconducting state. The transition temperature gives an idea about the quality of the sample. High and sharp transition temperature indicates a high quality sample, whereas lower transition temperature associated with a tail reflects bad quality and the existence of more than one phase [9,16].

There are two classical methods often used to determine the transition temperature. First, resistivity measurements; measuring the resistance (dc or ac) versus temperature. Second, magnetic susceptibility measurements; measuring the magnetic susceptibility as a function of temperature. Good quality samples also exhibit flux expulsion if the sample is field cooled (FC) and flux exclusion if the sample is zero field cooled (ZFC) [16].

3.2 Resistivity and Transition Temperature

The onset of superconducting transition is marked by the deviation of the resistance from its metallic linear behaviour. Zero resistance transition temperature (T_{C_0}) is identified when the resistance drops below 1 $\mu\Omega$.

Transition width (ΔT) has generally two definitions which are commonly used among many authors; namely, it is the difference between the onset and zero resistance transition temperature. It is also defined as the range of temperature where the resistivity drops from 90% to 10% of its value at the onset of transition. The second definition was employed in this work. The transition width (ΔT) determines the sharpness of the transition.

3.2.1 $Y_1Ba_2Cu_3O_{7-\delta}$ (Y_{123}) System

Fig. 3.1 shows a typical resistivity curve of the pure Y_{123} (near the transition region), the various definitions of the transition temperature (T_c) and the transition width (ΔT) used in this work are all illustrated on the figure. The results obtained for Y_{123} are : ($T_{onset} = 94.4K$ and T_{c_0} = 91.7 K) and the transition width ΔT =1.1 K. These results are comparable with best reported results of Y_{123} single crystals see [19,20].

3.2.2 $Y_{123}/(Ag_2O)_x$ Composites

Over the last two years many experiments have been conducted to study the properties of these superconducting / silver composites [18, 23,24]. Among these experiments there are some common results which encouraged us to use silver. Some of these results are:

1) Silver neither affects the orthorhombic crystal structure of Y_{123} nor reacts or replaces any of the Y_{123} constituents, at sintering temperatures less than 1200 K [18].

2) The existence of Ag provides a second phase with more pinning centers and therefore enhances the critical current density [23,24].

3) The decomposition of Ag_2O during the annealing process, into Ag and O_2 stabilizes the stoichiometry of Y_{123} specially the O_2 content [18].

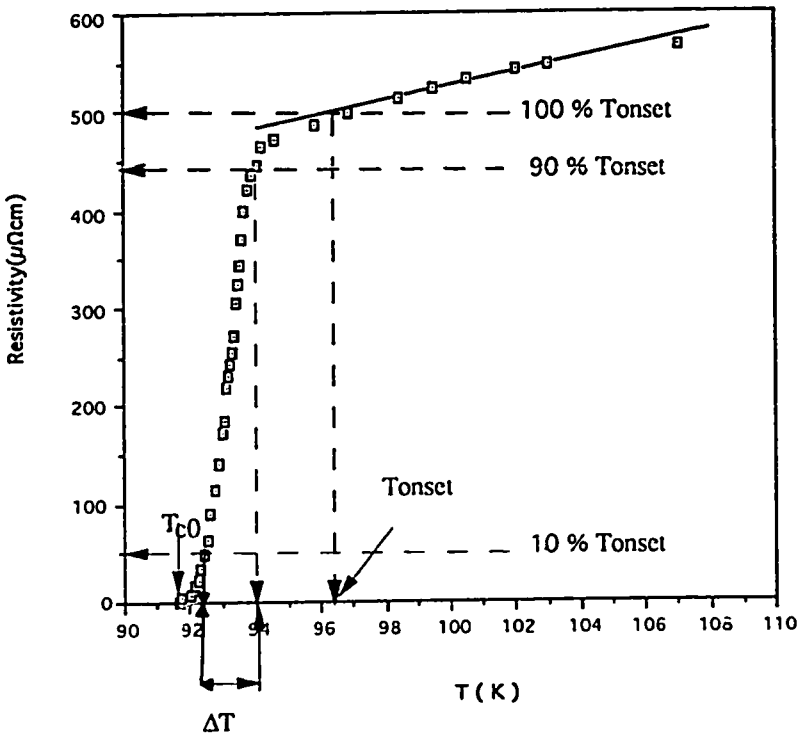

Figure 3.1: Typical resistivity curve of Y_{123} showing the various definitions of the transition temperature.

4) *Ag* fills the porosity and modifies the grain boundary and, therefore, reduces the effects of weak links. The electrical and thermal conductivities are increased above T_c [23].

5) Over a wide range of *Ag* concentration, its effect on the transition temperature is found to be moderate [18].

Moreover, Y. Shapira et al. [21] have reported that a (7:1) weight ratio of Y_{123}/Ag_2O (14.3% of Ag_2O) shows a much higher magnetization hysteresis losses than the pure Y_{123} or any other larger Ag_2O weight ratios. Moreover, the magnetization and hysteresis for this ratio (7:1) are found to be among the largest observed in ceramic samples. For this reason we decided to investigate this and other lower silver weight ratios. We embark on investigating the effect of silver on the transition temperature and width (in this chapter), critical current and pinning forces (Chapter 4) and flux flow resistance, viscous flow motion (Chapter 5).

The Y_{123} to Ag_2O weight ratios that we investigated were 7:1, 10.5:1 and 14:1 (the percentage of Ag_2O are 14.3%, 9.5% and 7.1% respectively). Fig. 3.2 (a & b) shows the variations of the resistivity with temperature for both pure Y_{123} and Y_{123}/Ag_2O with different concentration (x) of Ag_2OThe first noticeable important feature of Y_{123}/Ag_2O ceramic is the rapid decrease of the normal state resistivity (ρ_n) as the concentration (x) is increased from zero for pure Y_{123}. This decrease in the normal state resistance can also be seen in table 3.1, which lists the measured

values of ρ_n at both room temperature and at 100 K. To shed more light on this important property of Y_{123}/Ag_2O composites, a plot of the resistivity at 100 K, $\rho_{(100)}$, (near the onset of transition) versus the Ag concentration (x) is shown in Fig. 3.3. The figure shows that the normal state resistance is reduced from about 520 $\mu\Omega\,cm$ for $x = 0$ to about 300 $\mu\Omega\,cm$ for $x = 15\%$.

This behaviour can be understood as follows: above T_c, Ag grains mostly determine the behaviour of the resistivity of the sample. That is because Ag grains set between the Y_{123} grains and therefore fill the porosity there and since the conductivity of Ag is much higher than that of Y_{123}, the overall conductivity will be enhanced as the Ag concentration is increased [22].

Another important feature of the Y_{123}/Ag_2O composites (Fig. 3.2.b) is that Ag has a very little effect on the transition temperature (T_{c_0}). A plot of (T_{c_0}) versus x is shown in Fig. 3.4. Over the range of Ag concentration $x(0 - 15\%)$ the maximum change in T_{c_0} occurred is less than 1.5 K which is in fact consistent with the previous measurement done on this system [18,23]. Below T_c, the superconducting Y_{123} grains provide a better path for conduction. Therefore, the transition temperature remains approximately the same as long as a superconducting path exists in the sample. On the other hand any small reduction of the T_c could be attributed to the change in the coherence length as a result of the addition of Ag [22,23].

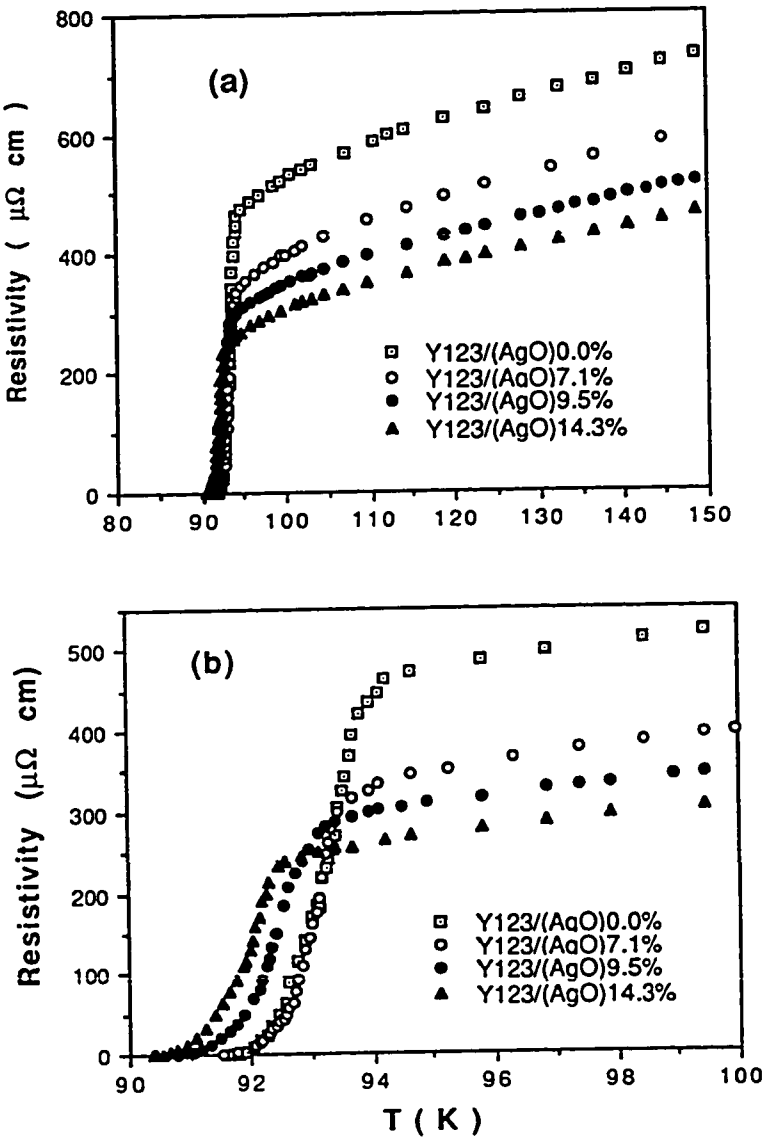

Figure 3.2: Resistivity of $Y_{123}/(Ag_2O)_x$ as a function of temperature for different Ag_2O concentration (x) (a) in the range (80-150 K) and (b) in the range (90-100 K).

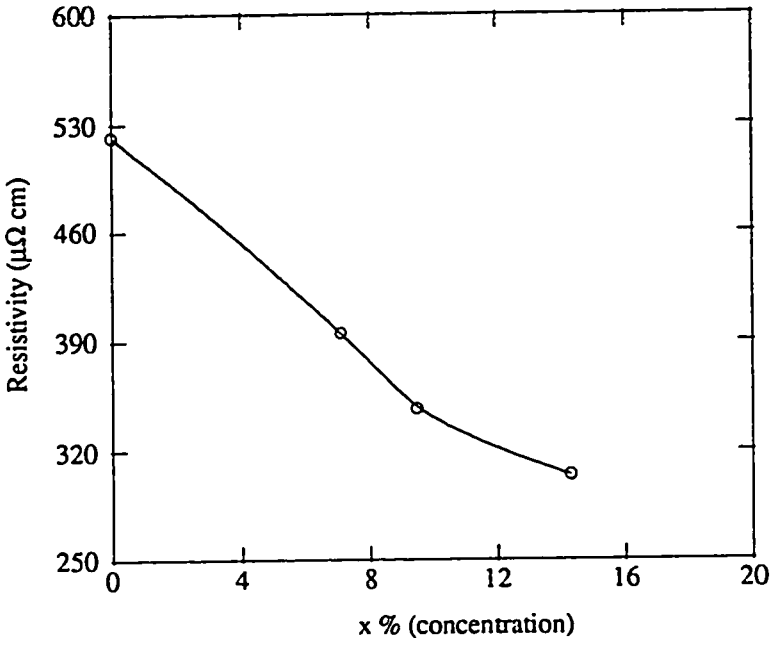

Figure 3.3: Resistivity at T=100 K as a function of Ag_2O concentration (x).

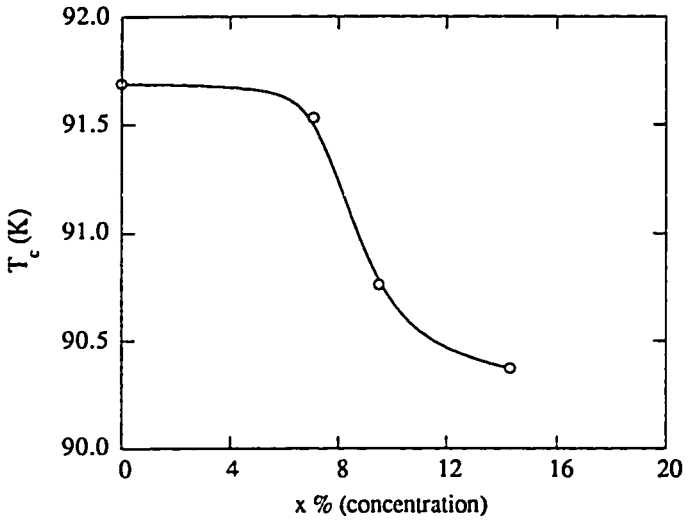

Figure 3.4: Zero transition temperature (T_{c_0}) as a function of Ag_2O concentration x.

Finally, the addition of silver also produces a little changes over the transition width (ΔT). This can be seen in Fig. 3.2.b by the small tail which appears at the end of the resistivity curve just before the resistance drops to zero. Fig. 3.5 shows the variation of the transition width (ΔT) as a function of $x(wt.\%Ag)$. It is clear that ΔT increases slowly as x is increased. This may be attributed to the existence of a proper new non-superconducting phase provided by the addition of silver.

Table 3.1 summarizes some of the most important properties of the system $Y_{123}/(Ag_2O)_x$ and compare the normal state properties such as ρ_{300}, ρ_{100}, $\frac{\rho_{300}}{\rho_{100}}$ and α (temperature coefficient) with pure silver. The ratio $\frac{\rho_{300}}{\rho_{100}}$ is almost constant for our system Y_{123}/Ag_2O indicating similar metallic linear behaviour for all Ag_2O concentration studied. On the other hand this ratio is small compared to that for pure Ag (almost half of that for silver). The temperature coefficient (α) was also evaluated using the relation $\alpha = \frac{1}{\rho_0}\frac{\Delta\rho}{\Delta T}$ and the results is listed in the table. We can see that α is constant for all concentration of Ag except for $x = 0$ it is a little bit smaller. On the other hand α for the system $Y_{123}/(Ag_2O)_x$ is smaller than that for pure silver.

3.3 X-Ray Diffraction Analysis

The crystal structure of all samples has been studied using the X-ray diffraction (XRD) technique. XRD patterns obtained for Y_{123} and $Y_{123}/(Ag_2O)_x$ composites indexed by comparing their patterns with standard published data for the orthorhombic structure. Almost all observed peaks have been identified and indexed according to the orthorhombic crystal structure except for a very few peaks with very low relative intensity ($< 1\%$). Within the sensitivity of our measurements, we did not see any reflections corresponding to any other phase in all

Table 3.1: Some important superconducting and normal conducting properties of $Y_{123}/(Ag_2O)_x$ compared to Ag pure.

X (Ag_2O wt.%)	T_{onset} (K)	T_{c_0} (K)	ΔT (K)	ρ_{100} ($\mu\Omega cm$)	ρ_{300} ($\mu\Omega cm$)	$\frac{\rho_{300}}{\rho_{100}}$	α (K^{-1})
0.0	94.4	91.7	1.1	522	1282	2.5	2.96×10^{-3}
7.14	95.2	91.5	1.3	394	1047	2.7	3.12×10^{-3}
9.52	94.1	90.8	1.4	347	925	2.7	3.12×10^{-3}
14.28	93.6	90.4	1.6	304	807	2.6	3.12×10^{-3}
$Ag(Pure)$			0.382	1.59		4.2	3.8×10^{-3}

$Y_{123}/(Ag_2O)_x$ composites as well as in pure Y_{123}For all $Y_{123}/(Ag_2O)_x$ composites, we could see two reflections of silver, namely, (111) and (200) reflections, which indicates the presence of silver as a metal in these composites. Fig. 3.6 shows the XRD patterns for the four samples studied, Miller indices identified for Y_{123} are marked on the Y_{123} diffraction patterns. Reflections corresponding to silver are marked by a stare (*).

Lattice parameters (a,b and c) for all samples have been calculated using a computer program (PDP, Powder Diffraction Package by M. Calligrais and S. Gevermita, University of Triesta, Italy). Miller indices for all observed peaks corresponding to the orthorhombic phase

structure along with their d-spacing values have been used as an input to the PDP program REFINE to calculate the lattice parameters. Results of M. A. Beno et al. have been used as a starting values of the lattice parameters for refinement program [29]. Calculated values of the lattice parameters for all samples along with their starting values and the standard deviation (σ) are shown in Table 3.2.

Lattice parameters changes are very small between pure Y_{123} and any $Y_{123}/(Ag_2O)_x$ composite on one side and among $Y_{123}/(Ag_2O)_x$ composites on the other side. No systematic changes could be identified (see Table 3.2). This again indicates that silver neither affects the orthorhombic crystal structure nor reacts or replaces any of the Y_{123} constituents, but stays as a metal setting between the Y_{123} grains.

Table 3.2: Calculated lattice parameters of Y_{123} and $Y_{123}/(Ag_2O)_x$ and standard deviation σ

X (Ag_2O wt.%)	$a(\AA)$	$b(\AA)$	$c(\AA)$	$\sigma(a)$	$\sigma(b)$	$\sigma(c)$
0.0	3.8193	3.8924	11.6798	0.0017	0.0018	0.0066
7.14	3.8318	3.9023	11.7423	0.0032	0.0032	0.0088
9.52	3.8316	3.8894	11.7215	0.0041	0.0040	0.0120
14.28	3.8063	3.8899	11.6607	0.0035	0.0038	0.0110
starting values	3.8231	3.8864	11.6807			

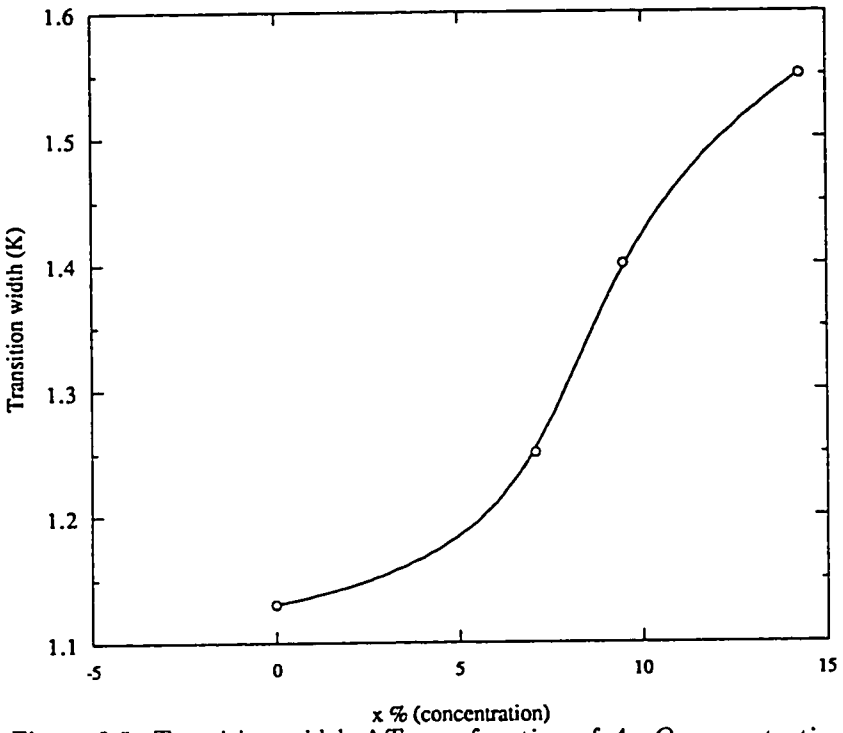

Figure 3.5: Transition width ΔT as a function of Ag_2O concentration x.

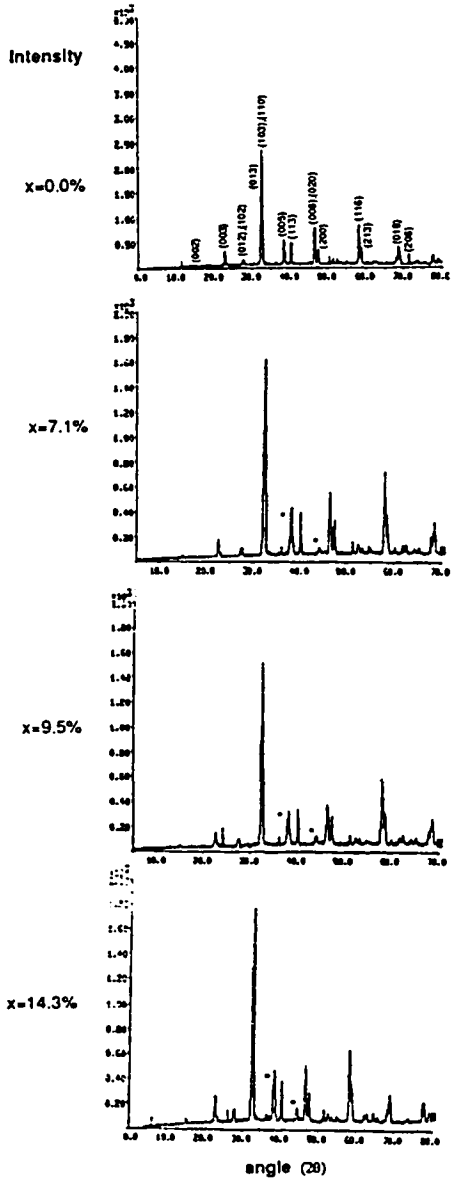

Figure 3.6: X-ray diffraction patterns of Y_{123} and $Y_{123}/(Ag_2O)_x$ composites. Reflections corresponding to Ag are marked by *.

Chapter 4

CRITICAL CURRENTS AND PINNING FORCES

4.1 Introduction

The magnetic behaviour of type-II SC below H_{c_1} is similar to that of type- I SC. As the applied field exceeds H_{c_1}, type-II SC goes into the trapped flux state (or a mixed state). In this phase it has been found that an ideal type-II SC (its magnetization curve is reversible) has a finite electrical resistance even at very low currents. This means that the critical current of an ideal type-II SC is zero and has been accounted for by Bean's critical state model [30]. However, most of type-II SC's are not ideal and can carry very high critical currents. Non-ideal SC's contain large amount of defects or impurities that serve

as pinning centers for the trapped flux lines.

A lower critical current is marked by the appearance of a voltage below T_c, and by a Lorentz force acting on the vortices, and when it exceeds the pinning force, the flux lines start moving. This motion will produce a sort of resistance called flux flow resistance which will be discussed in Chapter 5.

4.2 Critical Currents

In general there are many parameters affecting the critical current density (J_c) such as temperature, applied field, angle between the applied field, defects and impurities. In the case of Hi-T_c SC's the situation is even more complicated as there are more parameters affecting the critical currents. For example, the coherence length (ξ) in Hi-T_c is extremely small ($\sim$ *few* $\mathring{A}$) and consequently, Angstrom size pinning centers, or even atomic disorder will affect the critical currents and the dynamics of the vortices. Moreover, the critical current is also strongly influenced by the anisotropy of the layered structure of most of the Hi-T_c SC's. Since the structure of these copper-oxide materials is composed of layers ($Cu-O$) along $a-b$ plane and $Cu-O$ chains along c-axis. In fact the measured critical current density parallel to the $Cu-O$ is much higher than that measured along the c-axis [13].

In the present work, we will investigate the effect of temperature, field

and the addition of pinning centers (Ag_2O) on the critical currents and pinning forces in the Y_{123} Hi-T_c SC. In a perpendicular magnetic field, the critical current decreases rapidly at fields less than H_{c_1}. Between H_{c_1} and H_{c_2}, critical current vary with a smaller slope. In fact it is possible to deduce the values of the critical field (H_{c_2}) and thermodynamical equilibrium critical field (H_c) from the critical current measurements [38]. Even though, usually the critical fields can be obtained using the magnetization curves, critical current measurements offer another alternative method for obtaining the critical fields, pinning forces and their scaling behaviour [38,39].

4.3 Measurement Techniques

There are three different experimental techniques used to determine the critical current density; namely, transport or (I-V) characteristics, magnetization curves (hysteresis cycles) and the AC - susceptibility (through its imaginary part χ'') [31,32].

The magnetization method is an indirect way to determine the critical current. This method is used when it is difficult to form good contacts with the sample to carry out the transport measurements, like in the case of a small single crystal [1]. The critical state model is often used to determine the critical current density from magnetization measurements [30]. The critical state model makes use of the fact

that the magnetization of non-ideal type-II SC is reversible below a lower critical field H_{c_1}. As the magnetic field increases above H_{c_1} , the magnetization behaves irreversibly, and a critical current flows in the sample to prevent the penetration of the magnetic flux into the sample [1,13,16]. The critical current determined from the Bean model [30] is proportional to ΔM (hysteresis of the magnetization per unit volume) .

The most direct method used to determine the critical current is the transport method through the (I-V) characteristic, which is the method employed in our work.

The experimental technique used to obtain the (I-V) characteristic has been discussed in Chapter 2. The criterion used to define critical current densities is illustrated in Fig. 4.1 for a typical (I-V) curve of Y_{123} . At $T < T_c$ the current at which the voltage across the superconducting sample starts increasing linearly is called the lower critical current I_{c_1}.

This current is obtained by extrapolating the initial linear part of the (I-V) curve to the I-axis. The value of I-intercept is just I_{c_1}, below I_{c_1} the voltage is zero and is demonstrated by flux creep. In this region a thermal activation of the flux line may occur. The initial linear part of the curve above I_{c_1} is called flux flow region, and will be discussed in the next Chapter. The current I_{c_1} is called the intergrain current since it flows between the grains. At the end of the initial linear part there is a change of slope to lower values, this means that the motion of

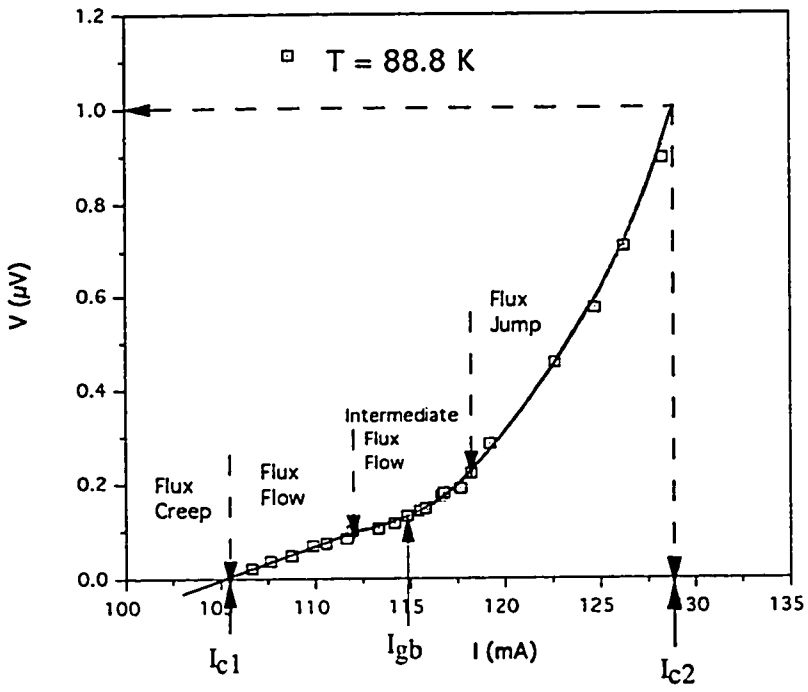

Figure 4.1: A typical (I-V) characteristic for Y_{123} showing the different critical currents associated with the different regions.

the vortices is slowed down. As a result of that a new current may be defined here which we call the grain boundary current (denoted by I_{gb}). This new region has been first observed in $(Bi-Pb)_2Sr_2Ca_2Cu_3O_{10}$ and called the intermediate flux flow region, it is associated with an inflection point [33].

As the current increases, the slope of the (I-V) curve starts increasing rapidly reaching the normal state resistance. This region is called the flux jump region, as the vortices are moving with high velocities, they are jumping over their pinning potential to the normal state. In this region a third critical current can also be defined which is called the upper critical current (I_{c_2}). The criterion used to define this current is a voltage drop of 1 μV caused by I_{c_2} . These different regions and the associated currents are all marked in Fig. 4.1.

The critical currents obtained from the (I-V) characteristics were found to be smaller than the corresponding values obtained from magnetization measurements in Y_{123} system [34]. This could be caused by granularity and integration contact, thus improving sample quality might bring transport current closer to their magnetization counterparts.

The (I-V) behaviour of type-II SC's depends on the way we introduce the magnetic field to the sample. Two types of measurements are customarily used to introduce the field.

a) Zero-field cooling (ZFC): the sample is cooled below T_c in the absence of a magnetic field, after that the field is turned on, then

measuring (I-V) characteristics. Under this condition the SC exhibits what is called diamagnetic shielding or flux exclusion, which means that the magnetic field fails to penetrate the sample.

b) Field cooling (FC): the sample is cooled below its T_c in the presence of the applied field, then measuring the (I-V) characteristics. Under this condition the SC exhibits what is referred to as the trapped flux state.

In the present work, we have used the second method (FC) to obtain the (I-V) characteristics at different temperatures and cooling fields. This has been done because most of the available experiments and results have been done using the first method (ZFC). In this Chapter we will discuss our results for such a measurement and compare the critical currents, pinning force and the flux flow resistance (will be discussed in Chapter 5) obtained by the two different methods.

RESULTS AND DISCUSSION

4.4 Critical Currents in Y_{123} System

4.4.1 Temperature dependence

It is a well established result that the critical current density is a decreasing function of the temperature for both classical and Hi-T_c SC's.

The value of $J_c(T)$ increases from zero at $T = T_c$ to a maximum value $J_c(0)$ at T=0 K. Fig. 4.2 illustrates some (I-V) characteristics of Y_{123} for different temperatures. The variations of the critical current densities J_{c_1}, J_{c_2} and $J_{c_{gb}}$ with temperature were plotted in Fig. 4.3. The critical currents start with a very small value near the transition temperature (T_c), then increasing almost linearly as the temperature is decreased. The initial slope $\frac{\Delta J_c}{\Delta T}$ is very small near (T_c), then J_c increases linearly with decreasing temperature ($\frac{\Delta J_c}{\Delta T} \sim$ constant). A small deviation from linearity occurs at lower temperatures. This initial linear increase in J_c is common to all Hi-T_c ceramic SC's, and is different from the quadratic behaviour commonly observed in classical SC's.

As the temperature decreases the (I-V) characteristics are no longer linear obeying Ohm's law, but instead they can be described in a power law (i.e $V \propto I^n$). A decrease in temperature results in an increase in the density of superelectrons which may causes this deviation from linearity. As a result the maximum current J_{c_1} increases rapidly below T_c. Similar behaviour can be found for $J_{c_{gb}}$ and J_{c_2}. This similarity is expected since the voltage associated with J_{c_1}, J_{c_2} and J_{gb} is almost constant and only a shift is occurred in the corresponding values of the critical currents.

Fig. 4.3 shows the critical current density as a function of T near the transition for the three different current densities. We are restricting our study to a range of temperature near T_c. Within this range,

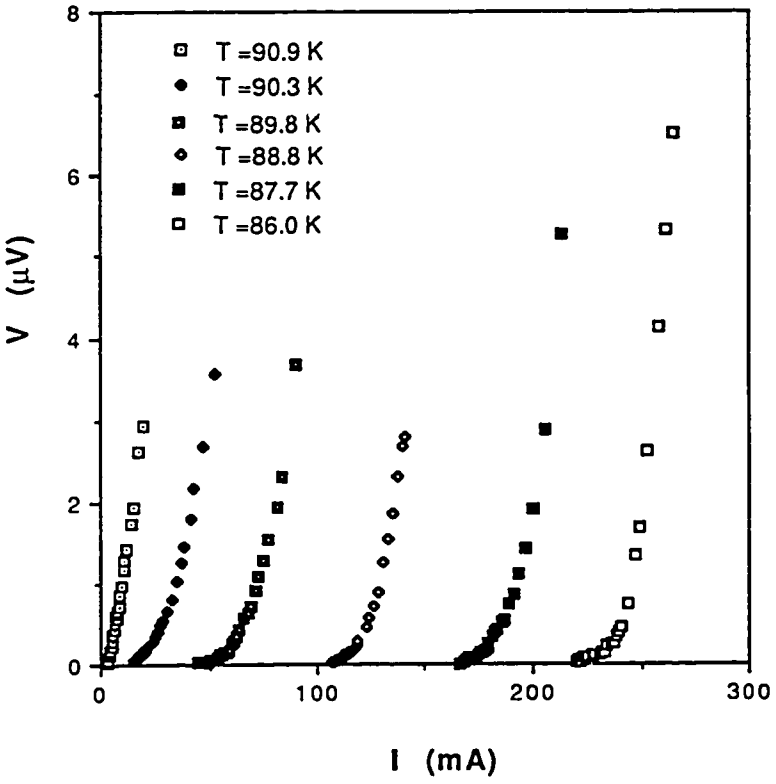

Figure 4.2: (I-V) characteristics for Y_{123} showing the effect of temperature on the critical currents.

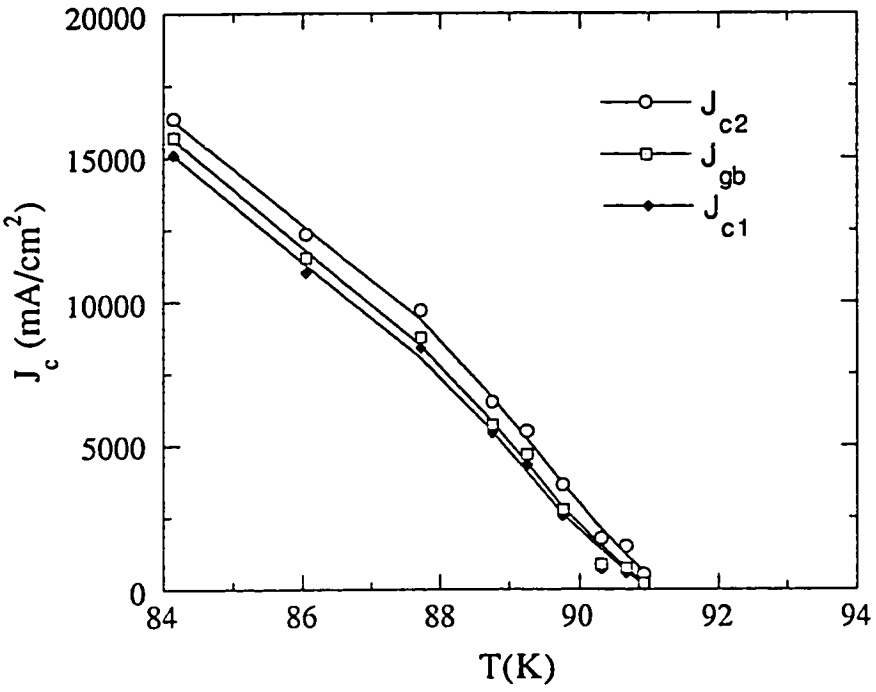

Figure 4.3: Critical current densities J_{c_1}, J_{c_2} and $J_{c_{gb}}$ as a function of temperature for Y_{123} system.

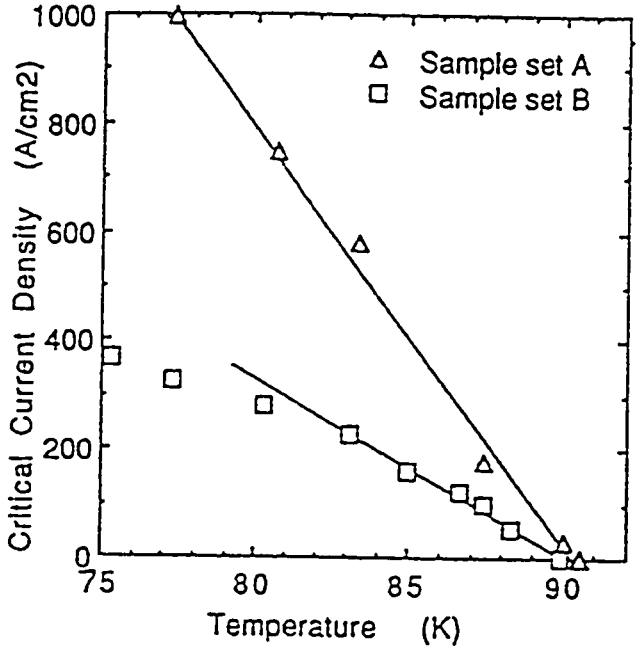

Figure 4.4: Critical current density as a function of temperature for two samples A and B for Y_{123}. Linear fits are shown for data close to T_c. (Thomas R. et al. [26])

superconducting-normal state transition occurs, and all superconducting properties change their behaviour, whereas at lower temperatures there is no radical change in many superconducting properties.

Our results regarding the behaviour of the critical currents near T_c agree with the available reported results on the Y_{123} polycrystalline materials. Fig. 4.4 shows the results of Thomas R. et al. for the linear decrease of critical current density versus temperature for two samples [26].

4.4.2 Magnetic Field Dependence

For conventional SC's in zero field cooled (ZFC) state the critical current density is a decreasing function of the applied field. The value of J_c decreases from a maximum value at B=0 to zero at $B = B_{c_2}$ (upper critical field) where the superconductivity breaks down. For our study, the sample was cooled in an applied magnetic field from above T_c to the measuring temperature. Magnetic flux lines will be trapped in the sample. The higher the cooling fields, the higher the trapped flux-line density inside the sample, and vortex-vortex interaction becomes more important.

Fig. 4.5 shows a representative (I-V) characteristics at one temperature (T=87.6 K) for different field cooled states. At low cooling fields (low flux-line density) the (I-V) behaviour is highly non-Ohmic . The critical current density decreases rapidly at first, as the cooling field increases (higher flux-line density), and the (I-V) curve starts approaching the linear (Ohmic) behaviour. Finally when $B = B_{c_2}$, (I-V) curve becomes linear with a purely Ohmic behaviour and the sample becomes normal. At such fields (near B_{c_2}) the vortices are overlapping with each other and the magnetic field penetrates the sample completely, destroying the superconducting state.

Fig. 4.6 shows J_c as a function of the field at different temperatures. The critical current density initially decreases rapidly with field ($B < 100G$) and then slows down at higher fields. These lower fields may

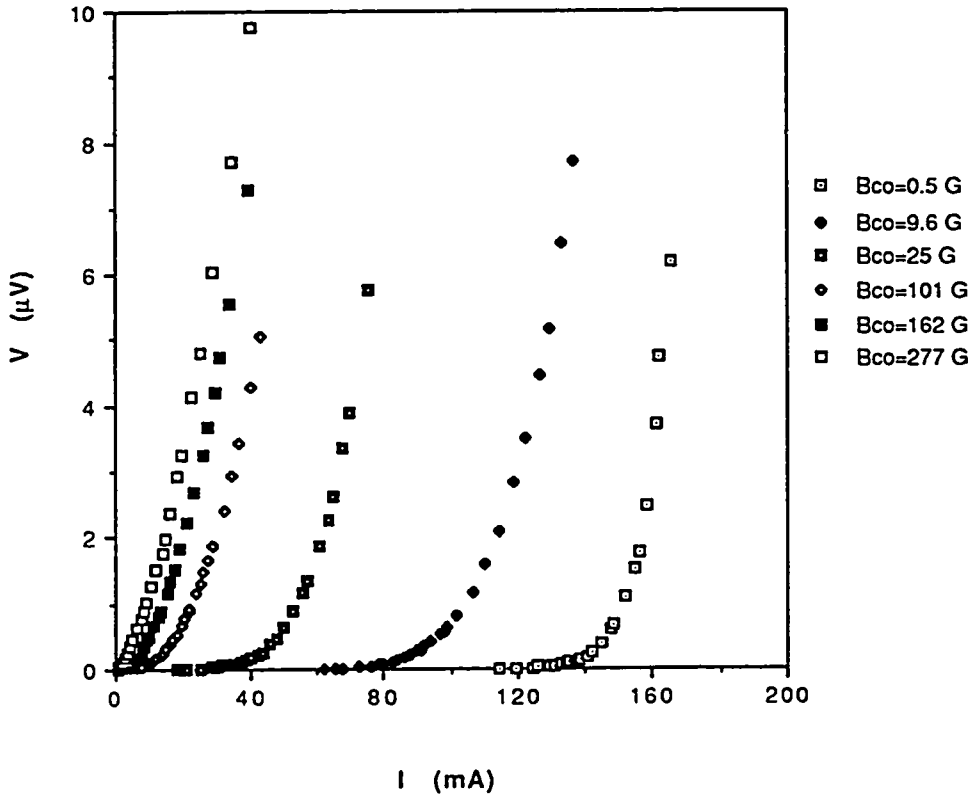

Figure 4.5: (I-V) characteristics for Y_{123} showing the effect of the cooling fields on the critical current density at temperature T=87.6 K.

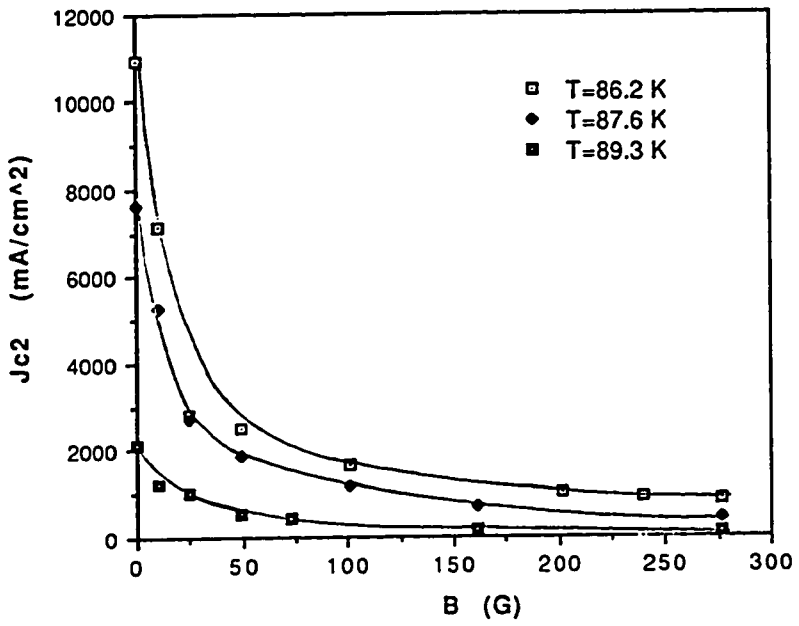

Figure 4.6: J_{c_2} as a function of the cooling field at different temperatures.

be identified as lower critical fields (B_{c_1}). Below B_{c_1} the SC is in a complete Meissner phase, and the low cooling field produces very low vortex density inside the SC and reduction in the current density with field represents a reduction in the screening current in the Meissner state [31]. At higher fields $B > B_{c_1}$, the field penetrates the sample, and as a result the screening magnetic currents J_m flow inside the sample. The reduction in the critical current (above B_{c_1}) reflects a reduction in J_m with increasing fields.

Most of the available results for the effect of the magnetic field on the critical currents were done using (ZFC) method. The (I-V) characteristics for different trapped flux states obtained by cooling the SC in different field have not been studied, and we were unable to find any detailed work on that. Thomas R. et al. [26] studied behaviour of the critical current at different temperatures for ZFC states. After increasing and decreasing the field (from zero to 1000 Oe and then to zero Oe again), the field cycling has resulted in a hysteresis in the critical current behaviour between the two states (see Fig. 4.7). The general behaviour of the critical currents for both cases (results of Thomas R. et al. and ours) is qualitatively similar. But it is not straight forward to compare the values of J_c's for the two different cases, because we have different samples prepared under different experimental conditions. Similar results regarding the behaviour of the critical currents for ZFC states can be seen in references [31,28]. The field dependence of the other critical currents (J_{c_1} and $J_{c_{gb}}$ as well as J_{c_2}) is shown in Fig. 4.8 at T= 86.9 K, they have almost similar behaviour.

The critical current densities determined from the (FC) method are in general larger than those determined from (ZFC) method. That is because of the trapped flux (pinned flux), since the SC will expels less flux in (FC) states than it excludes when (ZFC) (see Fig. 4.5).

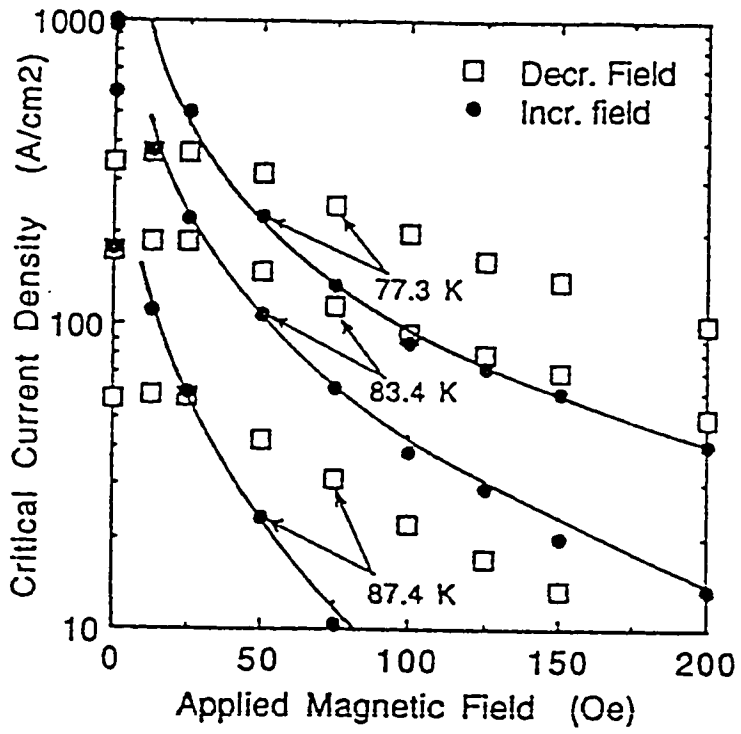

Figure 4.7: Critical current density versus applied field (ZFC) for field swept from 0 to 1000 Oe and back to 0. 1/H fits are also shown (after Thomas R. et al. [26])

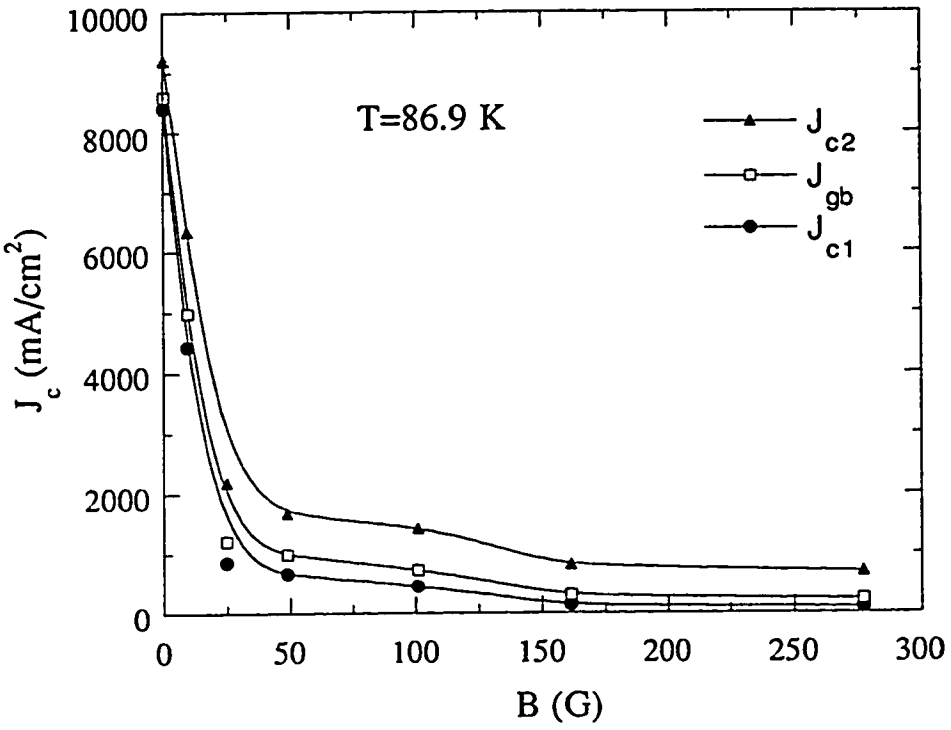

Figure 4.8: Different critical current densities as a function of the cooling field at T=86.9 K.

4.5 Order of Magnitude Calculations of the critical Fields

Critical current measurements as a function of the applied field can be used to determine the critical magnetic fields (B_{c_1}, B_{c_2} and B_c). The upper critical field B_{c_2} is the value of the magnetic field at which the critical current drops to zero. As it is shown in Fig. 4.6 the critical current density decreases rapidly at low fields and slows down at higher field. The decrease resembles that of an exponential function. From numerous examples reported in the literature on Hi-T_c SC it is found that at fields slightly higher than B_{c_1} the current density varies as $1/B^n$ with n generally ranging from 1 to 2. Moreover sometimes the field variation of J_c is even more rapid and approaches that of an exponential law [31]. A log-log plot of J_c versus 1/B is shown in Fig. 4.9 at different temperatures. The upper critical field B_{c_2}, can be determined by extrapolating these curves to zero current density. For temperatures 86.2, 86.9, 87.6, 89.3 and 89.8 K, the evaluated values of B_{c_2} are 80, 50, 20, 1.25 and 0.55 KG respectively. Moreover approximate values of B_c (thermodynamical critical field) can be deduced from Fig. 4.9. The figure shows a noticeable change of slope at fields close to B_c [27]. The estimated values of B_c from Fig. 4.9 are listed in Table 4.1.

The calculated values of B_{c_2} and B_c can be used to calculate the corresponding values of the lower critical field B_{c_1} and the G-L parameter

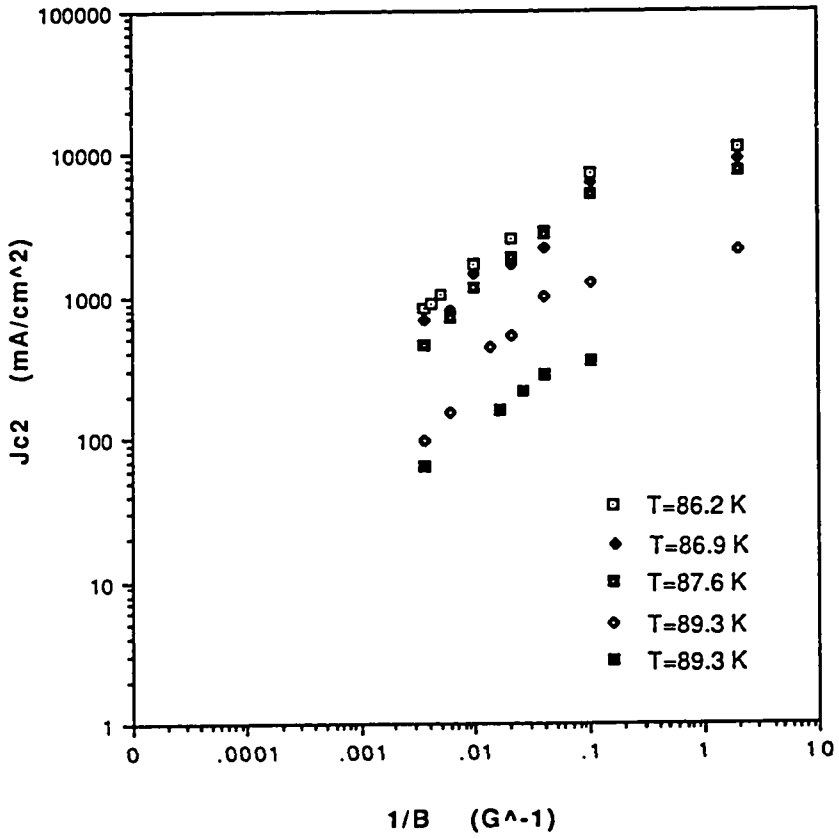

Figure 4.9: Upper critical current density J_{c_2} as a function of $1/B$ in a log-log scale.

Table 4.1: Values of critical fields B_{c_1},B_{c_2}, B_c and κ values at different temperatures for Y_{123} system

T(K)	B_{c_2} (KG)	$B_c(G)$	$B_{c_1}(G)$	κ
86.2	80	50	0.22	1130
86.9	50	42	0.16	840
87.6	20	36	0.39	390
89.3	1.25	18	1.00	50
89.8	0.55	10	0.65	40

κ using G-L equations

$$B_{c_1} = \frac{B_c \ln \kappa}{\sqrt{2}\kappa} \tag{4.1}$$

$$B_{c_2} = \sqrt{2}\kappa B_c \tag{4.2}$$

The calculated values of κ and B_{c_1} for different temperatures are listed in Table 4.1.

4.6 Critical Currents in $Y_{123}/(Ag_2O)_x$

We further investigated the effect of additional impurities: Ag_2O, on the critical currents in $Y_{123}/(Ag_2O)_x$ system. Critical current densities

are plotted as a function of Ag_2O concentration (x) (where x is the percentage wt. ratio) at temperature (T=86 K) in Fig. 4.10. The critical current densities increase with an increase in the concentration of Ag_2O as shown in Fig. 4.10. For example J_{c_2} at x=15 % is almost tripled compared to its value at x=0 % and the behaviour is approximately linear. Other values (J_{c_1} and J_{gb}) have similar behaviour but with smaller slope compared to J_{c_2}.

Fig. 4.11 shows the critical current density J_{c_1} as a function of the reduced temperature (T/T_{c_0}) for different AgO concentration (x). The plot is made versus the reduced temperature instead of the temperature itself in order to reduce the effect of small changes in T_c for the different AgO concentration (x). The behaviour of J_{c_2} and $J_{c_{gb}}$ was found to be similar to that for J_{c_1}, so only results of J_{c_1} are presented here. The general behaviour is linear decreasing function with T, reaching zero at $T = T_c$. The addition of AgO increases the slope as x is increased. This in fact indicates that AgO does not affect the superconducting properties of Y_{123} system too much, and it only enhances the pinning forces, which in turn enhance the critical currents.

4.7 Pinning Force

In the previous discussion (Chapter-1) of the flux-line motion induced by the Lorentz force, flux flow occurs when the driving force exceeds

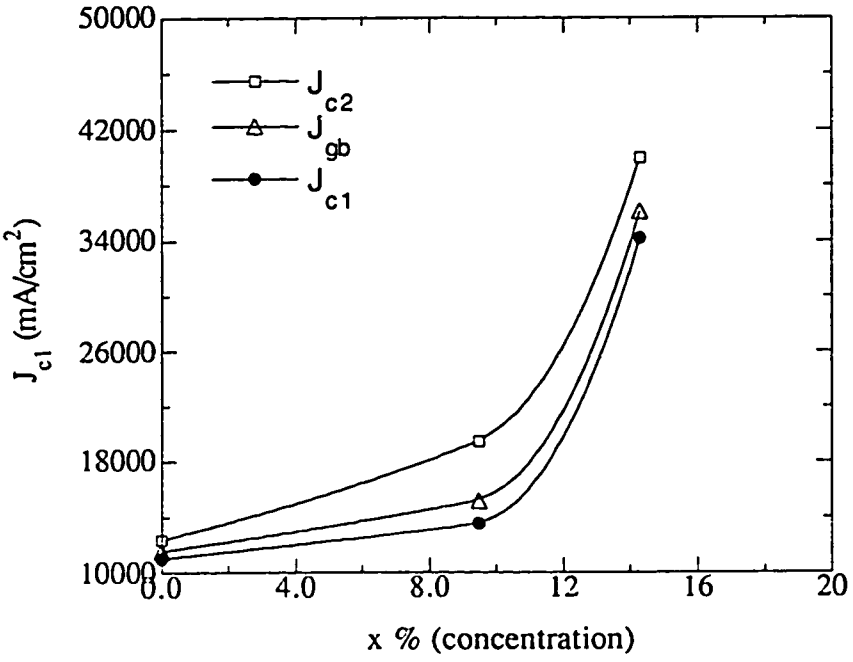

Figure 4.10: Critical current density as a function of Ag_2O concentration x (% wt. ratio) at T=86 K.

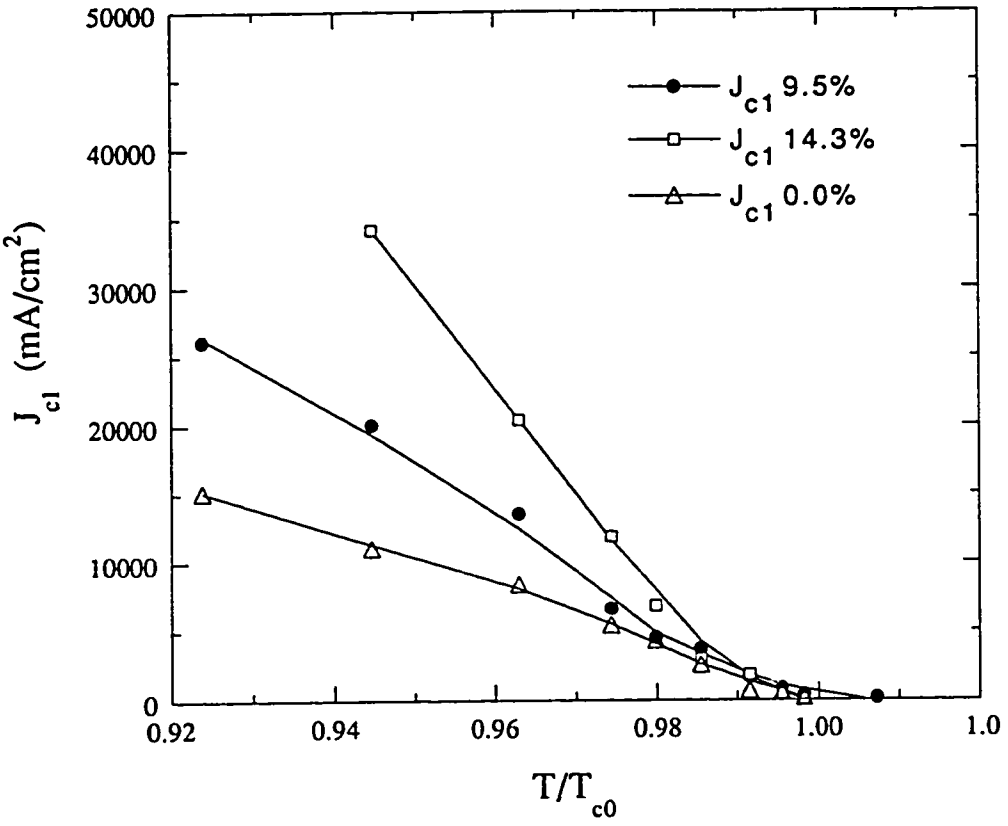

Figure 4.11: J_{c_1} versus T/T_{c_0} (reduced temperature) for different Ag_2O concentrations x.

the pinning force. Pinning forces can be determined from the critical currents; F_P is equal to the critical value of the Lorentz force. Flux pinning prevents the SC from reaching thermodynamic equilibrium, and causes irreversibilities in its magnetic behaviour.

The pinning force F_P is directed opposite to the flux flow velocity, and generally results from a local changes in the Gibbs free energy of the vortex lines. Such a potential well can be caused by metallurgical inhomogeneties in the material or by geometrical defects like sample edges, normal conducting precipitates (like silver-oxide in our case).

In Chapter-1 we have introduced the pinning forces f_P per unit length of the vortex line. It is often more convenient to introduce the force per unit volume by multiplying the force per unit length of the vortex line with the flux line density $n = \frac{B}{\phi_0}$ where ϕ_0 is the flux quantum. The pinning force per unit volume (or pinning force density) is then

$$F_P = n f_P \tag{4.3}$$

In its critical state, the SC carries the maximum current density everywhere, with minimum flux motion (flux creep). In the critical state the Lorentz force balances the pinning force; namely

$$\vec{F}_P(B) = (\vec{J}_c \times \vec{B})/c \tag{4.4}$$

where $(\vec{J}_c \times \vec{B})/c$ is the Lorentz force per unit volume [10]. This equation provides a way to determine the average volume pinning force

experimentally, since the critical current density can be determined experimentally at any temperature and field. In the present work this equation has been used to calculate the volume pinning forces for different temperatures and magnetic fields. Here we are mainly concerned with studying the behaviour of the pinning force for different trapped flux states (FC states). At a constant field, the pinning force is proportional to the current density. The behaviour of the pinning forces with temperature (at constant field) is similar to that of the critical current discussed in section 4.2.

4.7.1 The effect of the cooling Field on the Pinning Force

In Fig. 4.12 the volume pinning force F_P is shown as a function of the applied field for different temperatures. F_P has been calculated using the critical current data for J_{c_1} and equation 4.4. The pinning forces exhibit a peak with its position shifted towards lower fields at high temperatures. This peak is well defined at high temperature (for example T=89.3K). But at lower temperatures the peak gets broader. For example the peak at T=89.3 K is centered around B=20 G which approximately equals B_c at this temperature. Whereas at T=86.9 K the peak occurs at about B=100 G. Of course the pinning force will slowly decay as the field is increased and reaches zero at $B = B_{c_2}$.

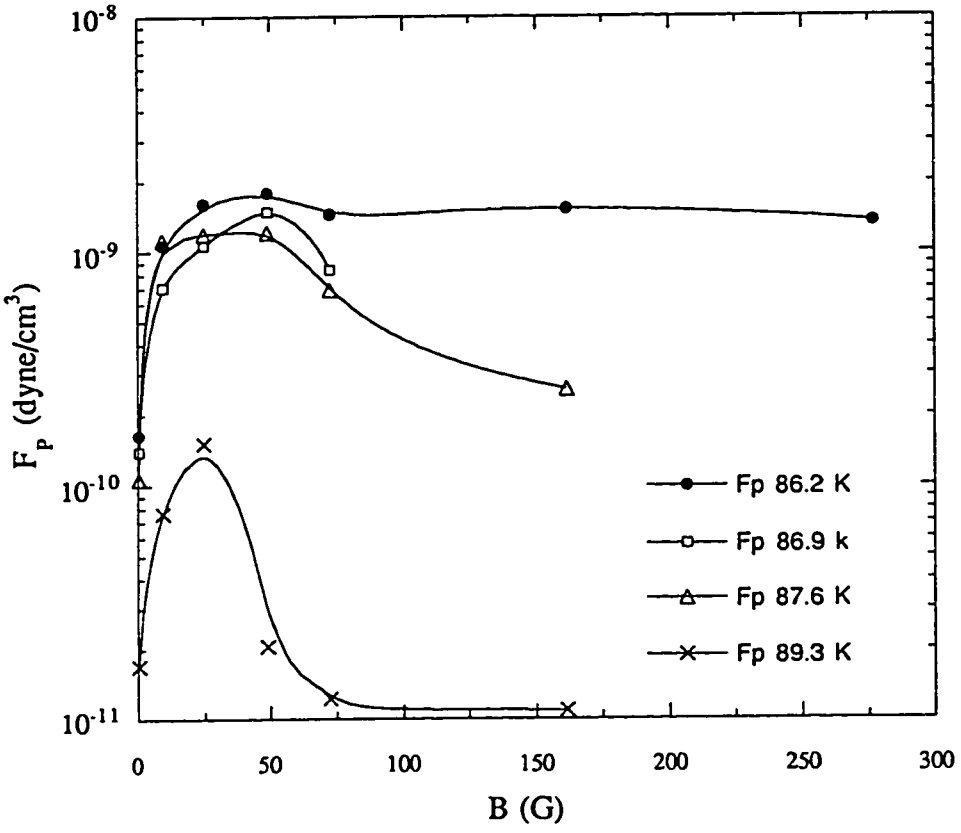

Figure 4.12: A semi-log plot of the volume pinning force as a function of the cooling field at different temperatures.

4.7.2 Scaling Laws for Flux Pinning

A major advance in the phenomenology of flux pinning was discovered by Fitz and Webb [40]. For a number of Nb-based alloys they found that the pinning force density (pinning force per unit volume) appeared to obey a scaling law of the form:

$$F_P = [B_{c2}(t)]^{2.5} f(b) \tag{4.5}$$

where f(b) is a function only of the reduced magnetic field $b = B/B_{c_2}$. The importance of this discovery is that, one could measure F_P at one temperature, and thus f(b) at this temperature and then immediately be able to predict F_P at other temperatures simply by the above scaling law [35]. The result of such a scaling laws is a universal curve or behaviour which is not limited to specific material. In fact many people have tried to apply the scaling laws, predicted by Fietz and Webb, to Hi-T_c materials and some of them have got good results [36,37,38,39].

To test the scaling behaviour of the FC-states in Y_{123} sample, a plot of the normalized pinning force ($F_P/F_{Pmax.}$) as a function of the reduced field (B/B_{c_2}) is shown in Fig. 4.13, where $F_{Pmax.}$ is the maximum pinning force observed at each temperature taken from Fig. 4.12 and B_{c_2} is the upper critical field listed in Table 4.1. It can be seen in Fig. 4.13 that most of the data points for the range of temperature used, fall on a single curve except for a few points which show some deviation from the curve.

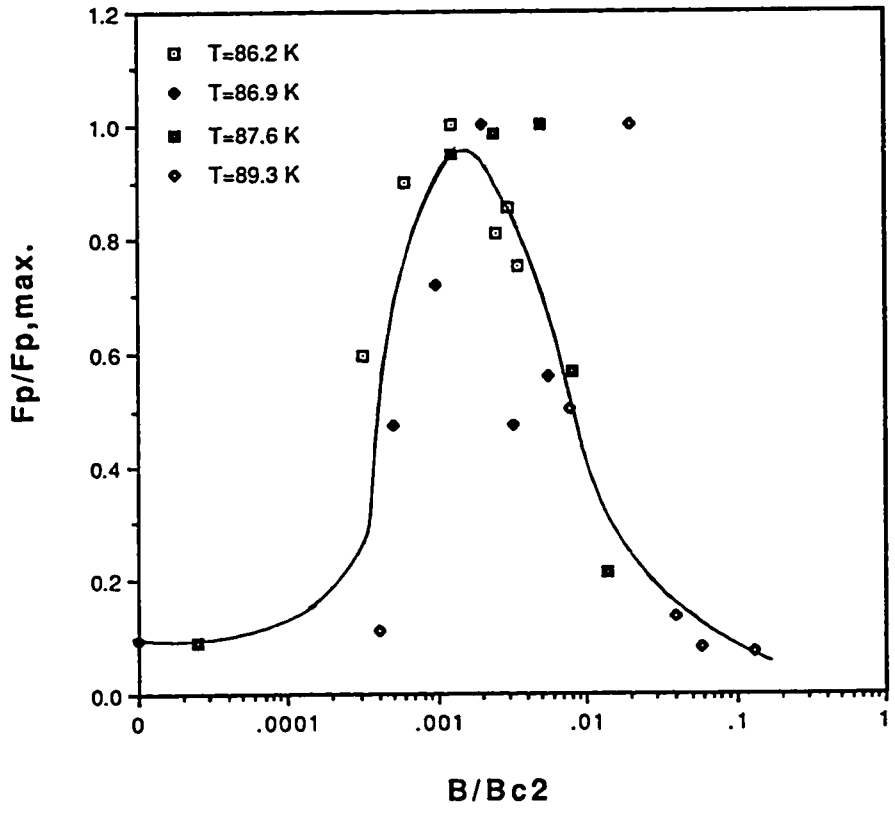

Figure 4.13: A semi-log plot of the normalized pinning force ($F_P/F_{Pmax.}$) as a function of the normalized field (B/B_{c_2}), showing a scaling behaviour of Y_{123} system.

There are many scaling laws that have been developed for Hi-T_c SC's based on the scaling laws created by Fietz and Webb for conventional SC (equation 4.5). The most commonly used one is [38]:

$$F_P = \alpha(D) B^n{}_{c_2} b^{1/2} (1-b)^2 \tag{4.6}$$

where $\alpha(D)$ is a function of the spacing of the strong pinning centers, $b = B/B_{c_2}$ and n is a constant that depends on the material. To calculate n, the log of F_{Pmax} is plotted versus the log of B_{c_2} as shown in Fig. 4.14. The data fall close to a straight line. The slope of the line gives the value of(if the pinning force is calculated from the definition $F_P = J_c \times B$ i.e without dividing by c, the speed of the light) n=1.4. Recently, L. W. Song et al. have preformed magnetic measurements and used similar scaling arguments for Y_{123} thin films, and obtained for (ZFC) state n=2.0 [39]. Also C. D. Wei et al. have tested the scaling laws for neutron-irradiated single crystals of Y_{123}, and they calculated the exponent n using the same method described above, they obtained a value of n=2.56 [38].

We have shown that our results regarding the pinning force follows a scaling behaviour. However, it seems that the scaling behaviour in ZFC and FC states may reflect the similarities and (or) differences between pinning mechanism for the flux lines in these states.

This phenomena and other related properties need more investigation. Currently we are pursuing such a study.

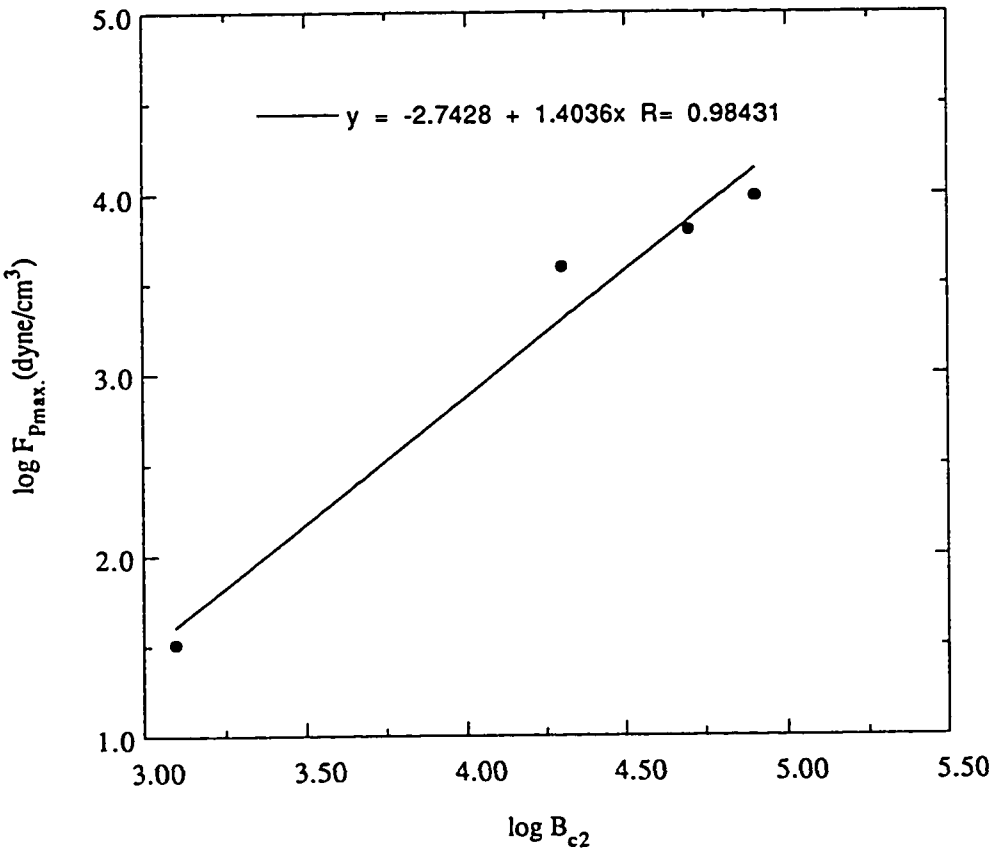

Figure 4.14: A log-log plot of the maximum pinning force as a function of B_{c_2}.

Chapter 5

FLUX FLOW RESISTANCE

5.1 Flux Motion and Flux Flow Resistance

In 1952, Shoenberg noted that the intermediate state, in type-I SC, becomes unstable when a transport current passes through it and the domains move in a direction perpendicular to the current and the applied magnetic field [10]. He appeared to have been the first to suggest the phenomenon of current-induced flux motion. However Gorter [10] was the first to propose flux flow as a resistive mechanism in type-I SC. Later, the concept of the flux motion was extended by Gorter and Anderson [10] to vortex lines in type-II SC's. However the first exper-

imental evidence for the appearance of the flux-flow resistance in the mixed state was obtained 1964 by Kim et al.[41]. Flux flow resistance appears in the mixed state of type-II SC when the critical current is exceeded, unlike what one would observe in type-I SC.

Consider a rectangular plate of a type-II SC in the mixed state which is held in a magnetic field perpendicular to both the plane of the plate and the current (I). As a result of the applied current and field, there will be a Lorentz force acting on the flux lines present in the plate given by

$$\vec{F_L} = I\vec{L} \times \vec{B} \tag{5.1}$$

where L is the length of the plate carrying the current. The direction of this force is perpendicular to both the current and the field. Since the flux is quantized, so the mean flux density is $B = n\phi_0$ where n is the number of vortices per unit area. Then the average Lorentz force on each vortex per unit length is (after dividing by the total length of all vortices present in the plate nLA):

$$\vec{F_L} = \vec{J} \times \vec{\phi_0} \tag{5.2}$$

where J=I/A is the current density and A is the cross sectional area of the plate.

The Lorentz force will set the flux-lines in motion in its direction. If the vortices are pinned to the impurities or defects of the material (hard

SC) the motion of the vortices will not begin until the Lorentz force overcomes the pinning force F_P, below this minimum value the vortices are stationary. Of course not every single vortex need to be directly pinned, but the interaction between the vortices is sufficient to give the lattice of vortices a certain rigidity. So if only few vortices are pinned, the whole lattice is immobilized. As long as the Lorentz force is less than the pinning force, there will be no motion except for that of the flux creep (which is a result of the thermally activated motion of the flux lines) [42,43,44]. If, however the transport current is increased so that $F_L > F_P$, the vortices start moving with velocity proportional to the difference $F_L - F_P$. The critical current density is reached at the moment $F_L = F_P$.

According to Kim's model, there is a viscous force that opposes the motion of the vortices through the sample, and therefore work must be done to maintain this motion. This work is supplied by the transport current and energy must be expended in driving this current through the SC. In other words, the vortices motion will be dissipative. There will be a voltage drop along the sample and therefore a sort of resistance will appear. The motion of the vortices is known as "flux flow" and it is the source of the observed flow resistivity [5].

5.1.1 Energy dissipation in the mixed state

Energy dissipation in a SC may take place as a result of two different processes. The first depends on the appearance of the local electric fields. This happens since the motion of the flux lines causes the magnetic field to change with time, as a result (and according to Maxwell's equations) an electric field will be generated. The electric field then accelerates the unpaired electrons inside the vortices, and they can pass their energy to the lattice and hence produce heat [1].

The second process depends on the spatial variation of the cooper-pair density in the vortex. When the vortices pass over a given point, the cooper-pair density n_s will change with time, n_s increases outwards from zero in the center of the vortex [1].

It should be stressed here that the criteria regarding the voltage is different in type-I and type-II SC's. In type-I SC, if the critical current is exceeded, the voltage is due to the transport current flowing through normal regions which span the whole sample. While in type-II, the material is still in the mixed state and there are still continuous superconducting paths threading the whole sample. In other words the voltage drop occurring in type-II SC is a direct result of the motion of the flux lines and it is a non-Ohmic behaviour. There are many experimental evidence regarding this issue [1,5,13].

5.1.2 Viscous force and viscosity coefficient

The (I-V) characteristics of the mixed state is independent of time. This means that the motion of the lattice of flux lines is uniform with constant velocity and there is no acceleration. This implies that the forces acting on the vortices must be balanced i.e the material in which they move exerts a viscous drag force. There will be a force F_v acting in a direction opposite to the vortex velocity v

$$F_v = \eta v \tag{5.3}$$

where η is the viscosity coefficient of the medium, and is related to the flux flow resistance.

According to equation 5.2 the Lorentz force acting on each flux line per unit length is given by $F_L = J\phi_0$. When this Lorentz force exceeds the pinning force, the flux lines start moving under the action of the viscous drag force according to the relation:

$$\eta\vec{v} = \vec{F_L} - \vec{F_P} \tag{5.4}$$

Since a power is required to maintain the motion with constant velocity (constant J), an electric field will be observed across the sample in the direction of I ,

$$\vec{E} = \vec{v} \times \vec{B} = n\vec{v} \times \vec{\phi_0} \tag{5.5}$$

now we can eliminate the pinning force from the problem (since it is an unknown quantity) by taking the derivative of equation 5.4 with

respect to F_L:

$$\frac{dv}{dF_L} = \frac{1}{\eta} = \frac{1}{\phi_0}\frac{dv}{dJ} \tag{5.6}$$

similarly take the derivative of equation 5.5 with respect to v:

$$\frac{dE}{dv} = B \tag{5.7}$$

and since

$$\frac{dE}{dJ} = \frac{dE}{dv}\frac{dv}{dJ} = \rho_f \tag{5.8}$$

thus the flux flow resistivity can be defined as:

$$\rho_f = \frac{B\phi_0}{\eta} \tag{5.9}$$

This expression offers an experimental technique to determine the coefficient η or ρ_f. Note that ρ_f is inversely proportional to η. If the damping of the medium increases, the flux lines move slower and a smaller resistivity results [41].

5.2 Kim's Model

In their investigation of flux flow resistance of type-II SC's, Kim et al. preformed (I-V) characteristics measurements for Nb-Ta alloys containing different amount of defects [41]. In there measurements, the voltage was measured in the direction of the current as a function of applied current and at a fixed external perpendicular field. For $F_L > F_P$, voltage V increases rapidly and becomes linear in I well above the critical

current I_c, indicating that $E \propto v$ as was assumed in equation 5.5. Moreover they found that the slope $(\frac{\Delta V}{\Delta I})$ in the linear region is constant and independent of the critical current and pinning forces. In other words the flux flow resistivity is the same whether the sample is pure or impure. This actually can be seen in the following way: since the driving force $F = F_L - F_P$ depends on the difference between I and I_c and not on I_c alone, i.e $F \propto (I - I_c)$ and therefore $v \propto (I - I_c)$. The voltage on the other hand, is proportional to v, so

$$V \propto (I - I_c) \tag{5.10}$$

hence

$$\frac{dV}{dI} = const. = \rho_f \tag{5.11}$$

This shows that the voltage V is independent of the pinning forces, i.e the pinning forces just shift the critical current [1].

For an applied magnetic field perpendicular to the sample, the flux flow resistivity increases with the field and approaches the normal state resistance as the field approaches B_{c_2}.

Kim et al. [41] have shown that the ratio of the flow resistivity to the normal state resistivity ρ_f/ρ_n follows an approximate relation which is independent of the alloy composition namely;

$$\rho_f/\rho_n = B/B_{c_2} \tag{5.12}$$

This simple relation leads to the following interpretation. If d is the average distance between flux lines, then $B = \frac{\phi_o}{d^2}$ (since each line carries only ϕ_o one flux Quantum) and $B_{c_2} = \frac{\phi_o}{\xi^2}$, hence

$$\frac{B}{B_{c_2}} = \frac{\xi^2}{d^2} \tag{5.13}$$

If we assume that the vortex core is a cylinder of normal metal of radius ξ, then the resistance ratio is equal the fraction of normal metal in the mixed state, and the mixed state resistance is due to the resistance of the normal cores [46].

At all temperatures ρ_f/ρ_n starts increasing linearly in B with constant slope. But of course, the range of B over which this relation holds decreases rapidly as $t = T/T_c$ increases. However, for sufficiently low field this relation holds independent of the temperature. At t=0, we expect this relation to hold all the way up to $B_{c_2}(0)$. In fact this suggests an experimental method to determine B_{c_2} at zero temperature. At zero temperature the ratio ρ_f/ρ_n increases linearly with field up to B_{c_2}, where it becomes constant.

In this chapter we will study the behaviour of the flux flow resistance and viscosity coefficient (η) for both system Y_{123} and $Y_{123}/(Ag_2O)_x$ as a function of temperature. Moreover, the behaviour of the flux flow resistance and the viscosity coefficient (η) in different trapped flux states will be investigated for Y_{123} system. Applicability of Kim's model for the two systems will be checked specially for the trapped flux states.

Scaling behaviour of ρ_f and η will also be discussed.

RESULTS AND DISCUSSION

5.3 Definitions

1. Flux flow resistance (FFR): is the resistance associated with the initial linear part above I_{c_1}. It is the resistance associated with the flux flow region marked on Fig. 4.1; it is calculated by evaluating the slope of the initial linear part just above I_{c_1}, (in I-V Curves).
2. Intermediate flux flow resistance (IFFR): is the resistance associated with the inflection point in the intermediate flux flow region defined in Fig. 4.1. This resistance is calculated using Ohm's low ($\frac{V_{gb}}{I_{gb}}$, where V_{gb} and I_{gb} is the voltage and the current associated with the inflection point.
3. Flux jump resistance (FJR): is the resistance associated with the flux jump region defined in Fig. 4.1. It is calculated from the slope of the (I-V) curve near $V = 1\mu$V. This resistance is expected to be close to the normal state resistance at the same temperature.

For clarity purposes, we frequently show some of our results. Occasionally, we omit some (I-V) curves, temperature or field scans. However these results are included when discussing general behaviours.

5.4 Y_{123} System

5.4.1 Temperature Dependence

Fig. 5.1 shows some (I-V) characteristics for Y_{123} measured at different temperatures. Just above the T_c the (I-V) curve is linear (Fig. 5.1-a) obeying Ohm's law since the sample is in its normal state. As the temperature decreases below T_c and at a given current, the associated voltage is reduced and the (I-V) curve deviates from linearity. In Fig. 5.1-b, we can distinguish four different regions: flux creep below I_{c_1}, flux flow, intermediate flux flow and flux jump above I_{c_2}.

The intermediate region is more clear in the range (110-170 mA) with a slope lower than that of (FFR). This indicates that the motion of the vortices is slowed down in this current range. Increasing the current in this range does not result in a pronounced increase in the corresponding voltage, it is almost constant ($\sim 0.1\mu V$). Finally, in Fig. 5.1-c the (IFFR) is now more clear, still it is occurring approximately at the same voltage ($\sim 0.1\mu V$) but it is shifted to the right on the I-axis. Clearly the slope associated with the (IFFR), in Fig. 5.1-c is less than the corresponding slope of (IFFR) Fig. 5.1-b.

In fact we have carefully investigated this region in the temperature range near the transition temperature through the (I-V) curves. We found that this region starts to develop near T_c and as the temperature decreases it becomes more pronounced over a large range of currents.

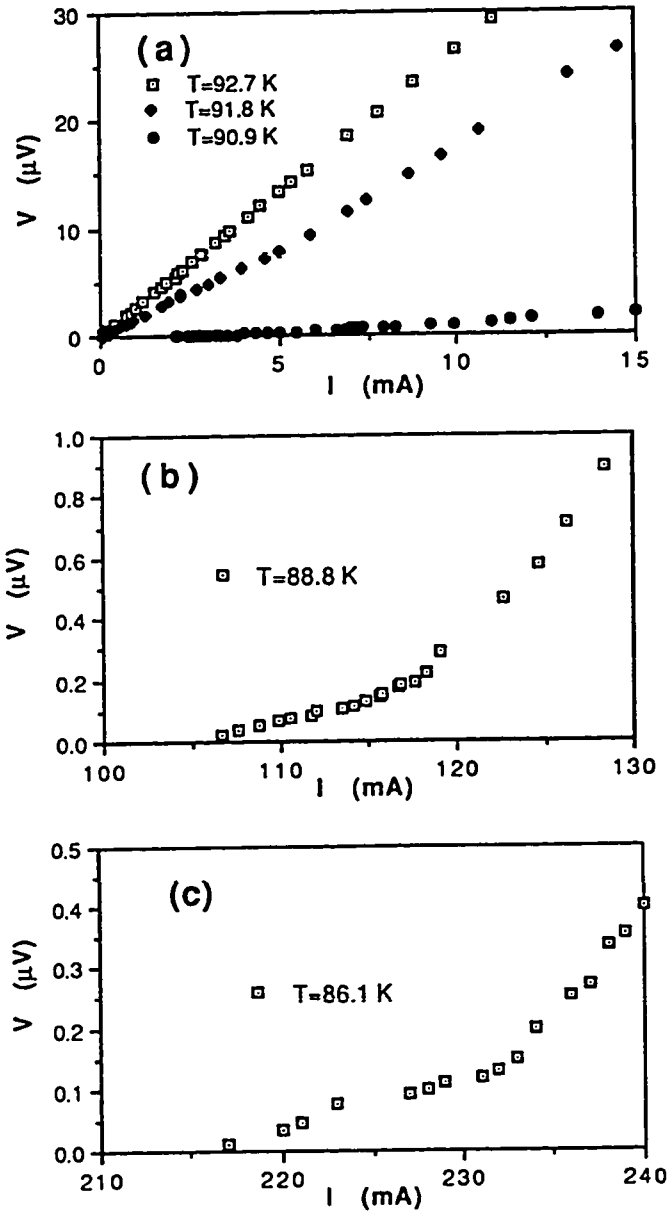

Figure 5.1: (I-V) characteristics of Y_{123} showing the behaviour of the different flux flow regions at different temperatures

Grain-boundaries might be the cause of the reduction in the (I-V) slope in this region. Detailed investigation of this region at lower temperatures is currently under consideration.

Fig. 5.2-a shows the variation of (FFR) and (IFFR) as a function of temperature. Both (FFR) and (IFFR) almost constant within the temperature range (84-92 K), but upon approaching T_c the resistance starts increasing rapidly , with FFR is always larger than IFFR. Flux jump resistance (FJR) exhibits similar behaviour (see Fig. 5.2-b), but of course with much higher values.

This diverging behaviour of FFR, IFFR and FJR has been investigated in $(Bi-Pb)_2Sr_2Ca_2Cu_3O_{10}$ Hi-T_c SC by Hamdan and Ziq , and was found to be similar to that obtained for Y_{123} [33]. It seems to us that this behaviour is a new feature of these copper-oxide SC's.
This behaviour is unlike what is expected from Kim's model [41]. At very low fields, as in our case, Kim et al. showed that the flux flow resistance is independent of the temperature.

5.4.2 Magnetic field dependence

The effect of the variation of the magnetic field on the FFR's was also investigated in the temperature range (80-90 K), the results at T=87.6K are shown in Fig. 5.3. Both FFR and FJR start at high value at (B=0.5 G), decrease with the field, and reach a minimum at

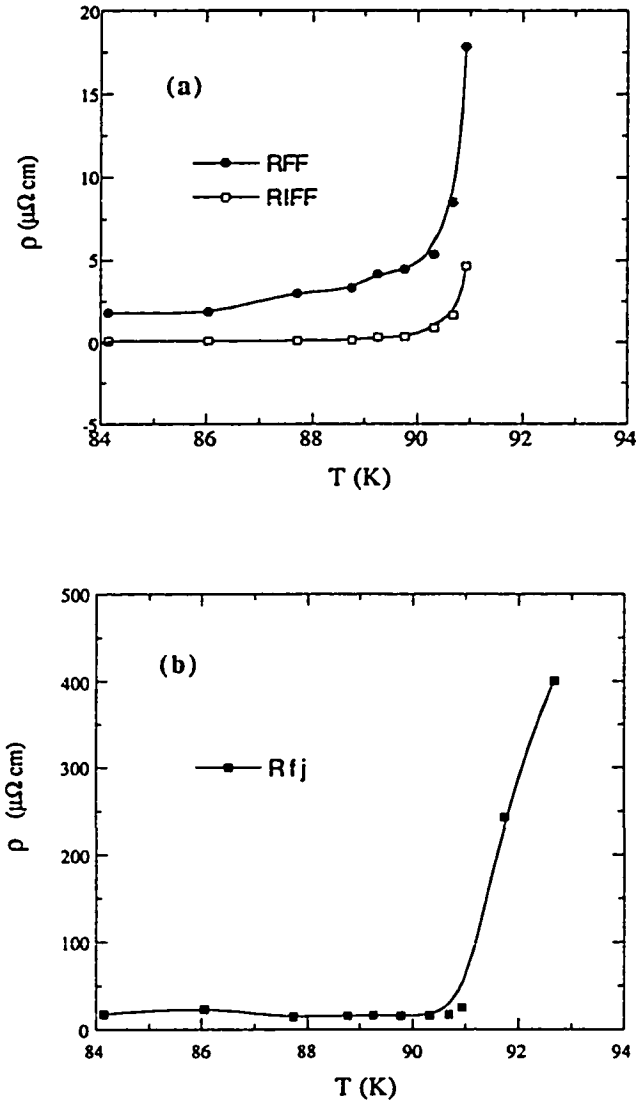

Figure 5.2: (a) FFR and IFFR, (b) FJR, as a function of temperatures.

about 10 G, then start increasing, approaching saturation at about 300 G. Whereas the behaviour of IFFR is somehow different , it shows a broad minimum around zero field, then increases slowly with field with zero initial slope. It also approaches saturation at about 300 G. Fig. 5.3-b reproduce Fig. 5.3-a but with a semi-log scale. It shows the initial variation of the resistivity, as well as its saturation behaviour.

Fig. 5.4-a shows the variation of the (FFR) as a function of the field at different temperatures. The dip in the resistance is still clear at all temperatures (86-90 K). The position of the dip decreases as the temperature is increased in this range. As the field is increased above 100 G the resistance is almost constant. However near T_c, the resistivity starts approaching saturation as the field increases above 100 G.

Fig. 5.4-b shows the variation of the FJR as a function of B at different temperatures. The behaviour is similar to FFR behaviour with B. The only difference is that the resistance dip at low temperature is shifted to higher fields.

Fig. 5.5 shows the normalized flux jump resistivity (FJR) as a function of the reduced field (B/B_c) where B_c is the critical thermodynamical field obtained from the critical current measurement (Chapter 4, Table 4.1). The resistance minimum at the lower temperature (T=86.2 and T=86.9 are shifted to a lower field ratio (B/B_c), reflecting that B_c increases, at lower temperature. The flux jump resistivity starts with the same initial slope for all temperatures ($B/B_c < 0.5$) and ap-

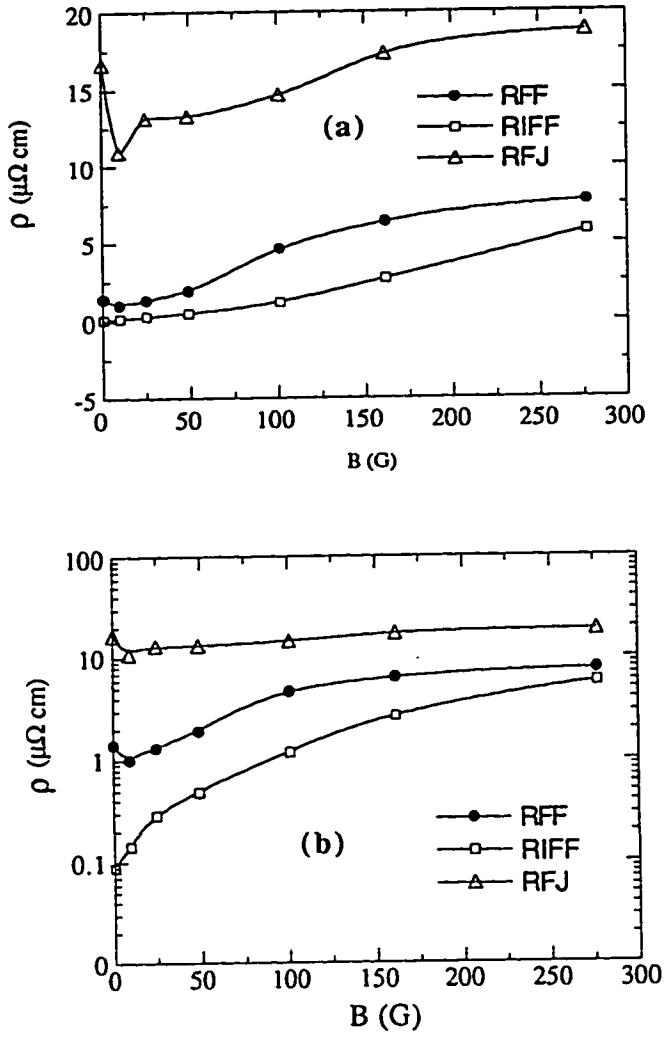

Figure 5.3: Flux flow resistivities versus B at T=87.6 K for Y_{123} system in different regions for (a) a linear scale and (b) semi-log scale.

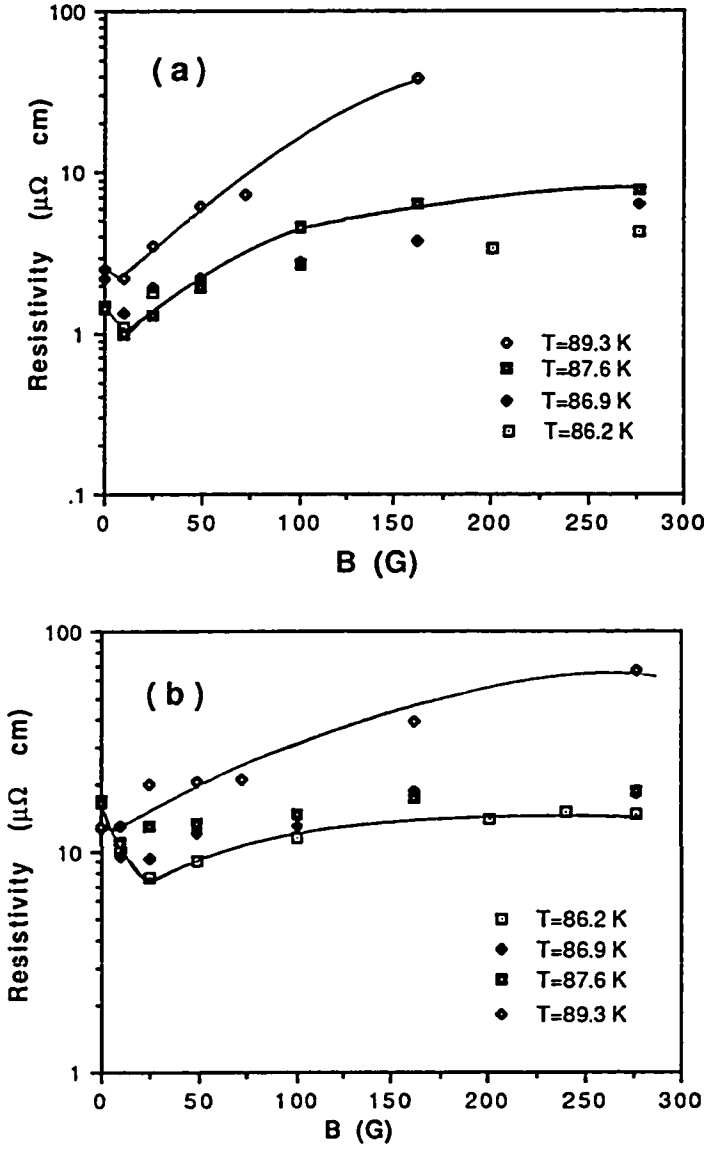

Figure 5.4: Flux flow resistivity versus field (B) at different temperatures on a semi-log scale in (a) flux flow region and (b) flux jump region.

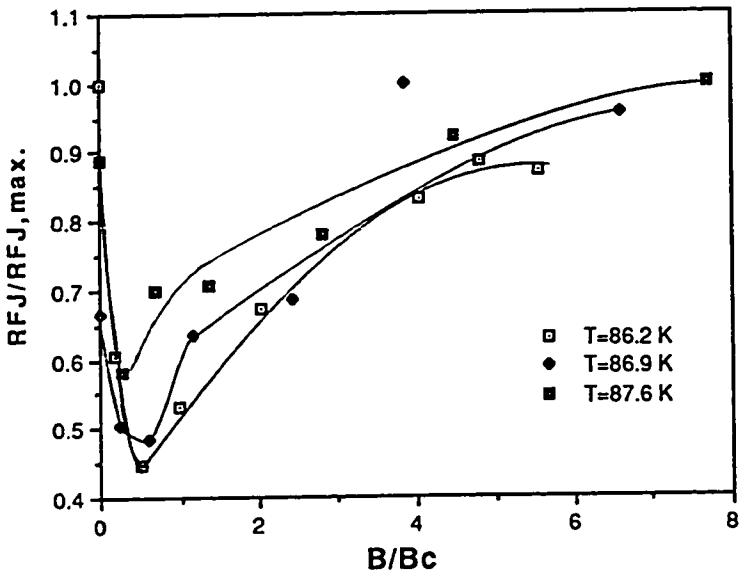

Figure 5.5: Normalized flux jump resistivity as a function of normalized field.

proaches saturation at higher field values ($(B/B_c > 4)$. It seems that the critical field used to reduce the field variable may play a decisive role in obtaining good scaling behaviour. We have tried to use B_{c_2} for this purpose, however the scaling behaviour got worse.

The resistance minimum has been investigated for conventional SC's; by Rosenblum et al. for Nb [48] and by Desorbo for Nb-alloys [47], and it has been found that the position of the minimum is independent of the current and field orientation. Moreover, the dip occurs at high fields (near B_{c_2}) where the magnetization vanishes. The critical current density also displays a peak effect at such fields (for Nb and Nb-alloys).

However it seems that the origin of the resistance minimum in Hi-T_c SC (as in our case) is quite different. No peak effect in J_c at B_{c_2} has been found , on the contrary J_c vanishes as $B \rightarrow B_{c_2}$. Also the dip occurs at low fields (less than 100 G), which are comparable to B_c which is much lower than B_{c_2} (see Table 4.1).

Finally, Fig. 5.6 illustrates the temperature dependence of the flux jump resistivity for different cooling fields. An interesting feature reflected in Fig. 5.6 is that (FJR) displays broad minima at lower fields (B= 0.5 G and B=9.6 G). The general behaviour of the variation in the resistivity as a function of temperature is the same as that discussed for zero field in the previous section. At low temperature and low field the resistance shows a clear broad minimum. As the field is raised the minima almost disappeared. The resistance starts increasing above T=87.5 K and diverges near T_c. For conventional type-II SC, Kim et al. have observed such a broad minimum in the flux flow resistivity versus temperature in the low field region. They attributed this resistance minima to the energy dissipation outside the vortex core.

Later on Clem investigated this broad resistance minimum and related it to the local temperature gradients in the vicinity of the vortex in order to account for the entropy changes resulting from flux line motion [45]. It would be very interesting to extend Clem's model to Hi-T_c SC (in the dirty limit and for very small coherence length ξ), incorporating both temperature and field effects (for both FC and ZFC) on entropy

changes resulting from vortex motion.

5.5 $Y_{123}/(Ag_2O)_x$ System

We further investigated the behaviour of FFR, IFFR and FJR upon increasing pinning forces in Y_{123}. As we have discussed earlier, silver content in Y_{123} increases these forces and enhances J_c values. Our results are included in Fig. 5.7 (a,c and c) which shows some (I-V) characteristics of $Y_{123}/(Ag_2O)_x$ where $x = 7.1\%$. The Fig. illustrates the different flux flow regions and how they vary with temperatures similar to what we have seen for Y_{123}.

In Fig. 5.7-a the line with higher slope is just above the transition temperature shows no deviation from linearity whereas the other one (at temperature within the transition width) shows very small deviation from linearity.

Fig. 5.7-b shows 4-different regions namely; flux creep, FFR, IFFR and FJR. The temperature here is just below the T_{c_o}. On comparing the IFFR in Fig. 5.1 for (pure Y_{123}) and in Fig. 5.7, we notice that the voltage associated with this region is now lower than that associate with Y_{123}. Fig. 5.7-c illustrates (I-V) curve at relatively lower temperature ($T = 85.3K$). The IFFR is now very clear, and very broad extending over a large range of current (370-460 mA).

5.5.1 temperature dependence

We have seen that the addition of Ag_2O reduces the normal state resistance (Chapter-3). We further investigated its effects on FFR, IFFR and FJR. They all have similar temperature behaviour. Fig. 5.8 shows the variation of FJR with the reduced temperature (T/T_{c_o}) for different Ag_2O concentration (x). The general behaviour of the flux flow resistivity for all Ag_2O concentration is similar to that of pure Y_{123} in the sense, that at low temperature is almost constant and then upon approaching T_c it starts increasing rapidly. the broad minimum is shifted to a lower temperature. The main feature is in the difference in the constant value of FFR and FJR. For pure Y_{123} (x=0) FFR, IFFR and FJR are at least one order of magnitude higher than that obtained for any other concentrations.

The behaviour of FFR, IFFR and FJR is illustrated in Fig. 5.9 as a function of x at T=87.6 K. Similar behaviour at other temperatures ($< T_c$) has been found.

This reduction in the flux flow resistance as a result of silver addition is unlike what is expected from Kim's model. Kim has found for classical type-II SC's that the flux flow resistance is independent of the critical current of the sample, and the pinning forces, or equivalently independent of the amounts of defects. However in our case we have found that the addition of silver enhances the critical currents and reduces the flux flow resistivity.

5.6 Viscosity Coefficient (η)

5.6.1 Y_{123} System

Temperature dependence

It was pointed out at the beginning of the Chapter that as the Lorentz force F_L exceeds the pinning force F_P, the creep flux motion ($F_L < F_P$) of the vortices converted into a viscous motion according to equation 5.4

Moreover η is the viscosity coefficient which is related to the flux flow resistivity as

$$\eta = \frac{\Phi_0 B}{\rho_f c^2} \tag{5.14}$$

thus measurement of ρ_f yields the viscosity coefficient η. We have used the measured values of ρ_f in different regions and under different conditions to calculate η using the above equation. The results are given in Fig. 5.10, which shows the temperature dependence of η in different flux flow regions for Y_{123} plotted in a semi-log scale. Initially at high temperature near the transition temperature, the viscosity coefficient (η) starts with very small values, increases rapidly as the temperature decreases, then develops into a broad maximum (for very small fields and low temperature) . This behaviour is just what one expects from the variations of the FFR versus temperature (compare with Fig. 5.3), (note that $\eta \propto \frac{1}{\rho_f}$ or $\eta \propto \sigma$; conductivity). The maximum of η in the flux jump region (HFJ) (we are using H instead of η, so for

example: HFJ represents the viscosity coefficient η in the flux jump region) is broader than that of HFF or HIFF, its saturation persists up to a higher temperature (close to T_c). The highest damping effects (max. η) occurs in the intermediate region and the lowest occurs in the flux jump region, whereas in the flux flow region values of η are lying between these two extrema.

The damping effects of the medium is reflected in the behaviour of its viscosity coefficient, and represents a retardation mechanism in the motion of the flux lines. Therefore the resulting velocity of the flux flow will decrease as η increases, the induced voltage also decreases, hence flux flow resistance of the medium will be decreased.

Effect of the field

Fig. 5.11 shows the effect of the field on the viscosity coefficient (η) at constant temperature ($T = 87.6K$) for different flux flow regions (HFF, HIFF and HFJ). At very low field, η starts with very small values and then increases quickly as the field is increased passing through a broad maximum for HFF and HFJ, a much sharper peak is obtained for HIFF.

The viscosity coefficient is expected to go to zero at very high fields ($B \sim B_{c_2}$) which quenches the superconducting state. The behaviour of the viscosity coefficients HFF, HIFF and HFJ at different temperature has also been investigated (see Fig. 5.12). At temperatures close to

T_c, η exhibits a maximum at low fields ($\sim 50G$) (as in the case of $T = 89.3K$). At lower temperature the peaks shift to higher fields (only HFF is shown in Fig. 5.12)

As the field increases from zero, the density of the flux lines per unit area increases and therefore the distance between the flux lines decreases until they finally overlap at fields very close to B_{c_2} (when the distance between the vortices is comparable to ξ). Since the core of these vortices is in the normal state we expect that the percentage of the normal phase in the superconducting sample to increase as the field increases and η is expected to become very small.

At low temperature the values of the critical fields B_{c_2} at which superconductivity is quenched are higher, therefore we expect also the values of the critical field at which η is maximum, to be higher. So this maximum will be shifted to higher fields. This agrees qualitatively with our results shown in fig. 5.12 for the viscosity coefficient in the flux flow region

We further investigated the universal scaling behaviour of the viscosity coefficient, trying to obtain generalized behaviour as a function of reduced field. Fig. 5.13 shows a semi-log plot of the normalized flux jump viscosity coefficient ($HFJ/(HFJ)_{max.}$) as a function of the cooling field at different temperatures. An interesting feature reflected in this figure, is that all the points from different temperature fall on the same curve, which suggests a scaling behaviour in this range of the field

(0 - 300 G) .

Fig. 5.14 shows the normalized HFF versus the field at different temperatures. However, the scaling behaviour is not clear in this plot. We have explored other scaling argument for HFF and HIFF. This is vividly shown Fig. 5.15, which reveals the normalized HFJ as a function of the reduced field (B/B_c) where B_c is the thermodynamic critical field listed in Table 4.1. In this Fig. we could notice also a scaling behaviour. The viscosity coefficient in this region increases linearly with field and then reaches saturation at higher fields.

We have tried to investigate the scaling effect in the different regions using the upper critical field B_{c_2} as a reduced field instead of B_c, but we didn't notice any scaling behaviour in any of the flux flow regions. Currently we are exploring these and other scaling arguments in all flux flow regions.

5.6.2 $Y_{123}/(Ag_2O)_x$ system

Temperature dependence

Fig. 5.16 shows a semi-log plot of (HFF) as a function of the reduced temperature for different Ag_2O concentration (x). In the flux flow region at temperature very close to T_c , η decreases as the temperature approaches T_c for all (x), and η is almost constant at low temperature. An important feature in this figure which is worth noting is that the

minimum damping effects occurs for pure Y_{123} at ($x = 0$), and (η) increases at $x = 7.1\%$ but then it decreases for the other two concentrations. The increase in η is about two orders of magnitude larger when compared with that for pure Y_{123}.

However the behaviour of the viscosity coefficient in the flux jump region shown in Fig. 5.17 is different from that in Fig. 5.16 in two aspects:-

1. The difference between the values of η for $x = 0$ and other concentrations is large, but there is no much difference among the η values for different concentrations with ($x > 0.0$)
2. η in this region exhibits a maximum at temperature close to T_c for ($x > 0.0$) only

Otherwise the global behaviour is the same in the two regions and also for that in the intermediate region (not shown here). Note that Fig. 5.16 is plotted on a semi-log scale, whereas Fig. 5.17 is not (linear-scale).

In order to get a better idea about the effect of silver on the viscosity coefficient, we found it interesting to look at this effect at one fixed temperature. For this purpose Fig. 5.18 shows the variations of η in different regions as a function of the concentration (x). We could see that in the flux jump region, η increases initially slowly between (x=0 and x=7.1 %) and then saturates. Whereas in the other two regions it

increases faster, goes through maximum at x=7.1% but then decreases with x.

For conventional type-II SC's, through his theoretical model, Clem was able to show that the viscosity coefficient versus temperature exhibits a broad maximum [45]. In this model he added to the empirical low field viscosity coefficient $\eta(T)$, studied experimentally by Kim et al. a new term $\eta_{th}(T)$, in which he included the effect of dissipation arising from local temperature gradients in the vicinity of vortex cores. He also pointed out that this maximum in η could be observed for impure SC's only (i.e the peaks becomes sharper as impurity increases), and it becomes less pronounced with increasing purity and disappears completely if the mean free path exceeds certain limit $l \geq 1/4\xi_0$. In fact this seems to be in agreement of our results. From Fig. 5.17, we can see that the maximum almost disappeared in the case of pure Y_{123}, which is considered to be more pure compared to $Y_{123}/(Ag_2O)_x$. Whereas this peak is well defined in the case of (x=14.3%), but less pronounced for the other two concentrations (x= 7.1% and 9.5%) in accordance with Clem's model [45].

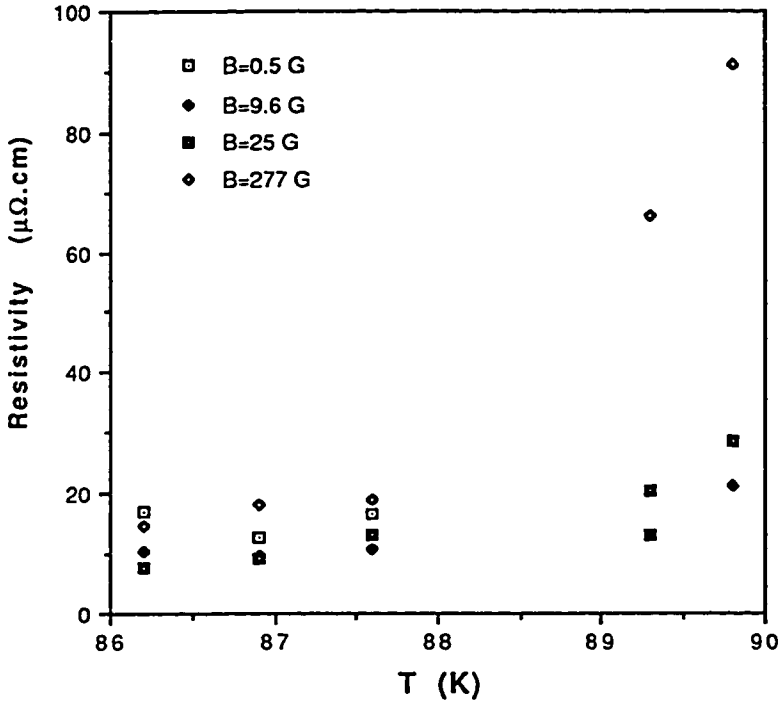

Figure 5.6: Flux jump resistivity (FJR) vs. temperature for different fields.

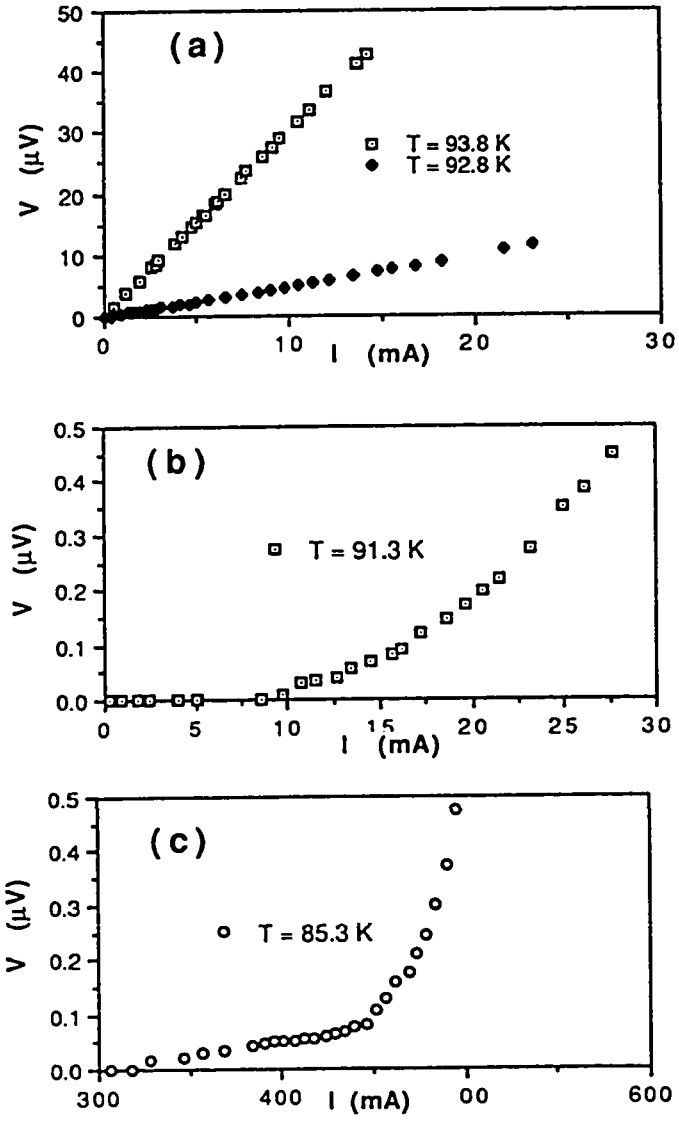

Figure 5.7: Some (I-V) characteristics for $Y_{123}/(Ag_2O)_x$ system (x=7.1%) showing the different flux flow regions.

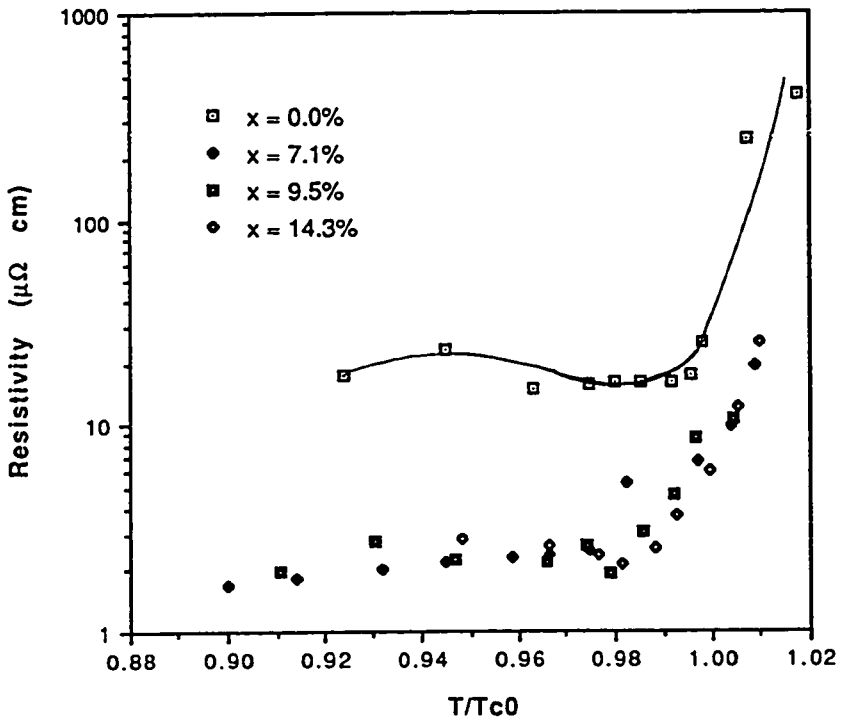

Figure 5.8: FJR vs. the reduced temperature (T/T_{c_o}) at different Ag_2O concentration x.

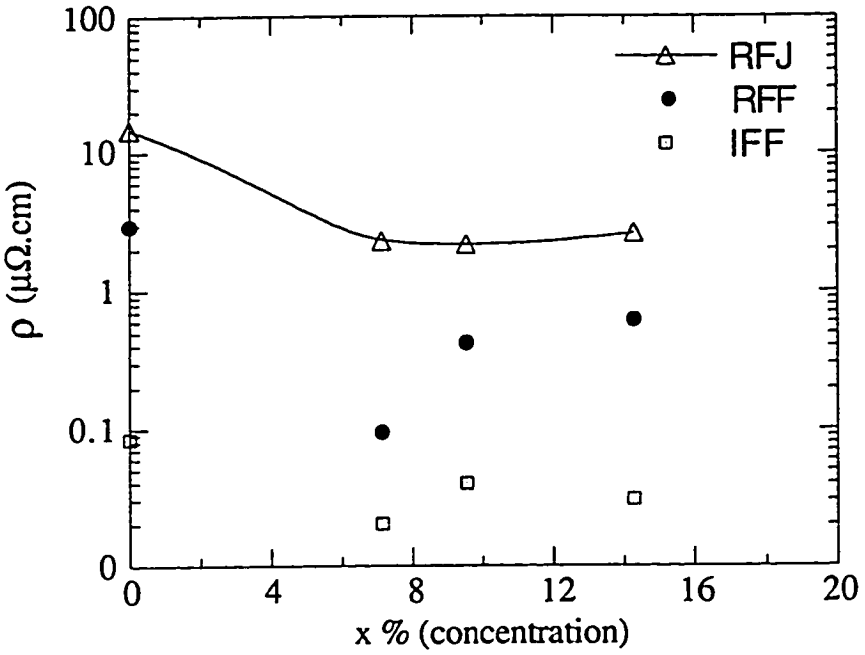

Figure 5.9: Flux flow resistivity in different regions vs. Ag_2O concentration x at T=87.6 K.

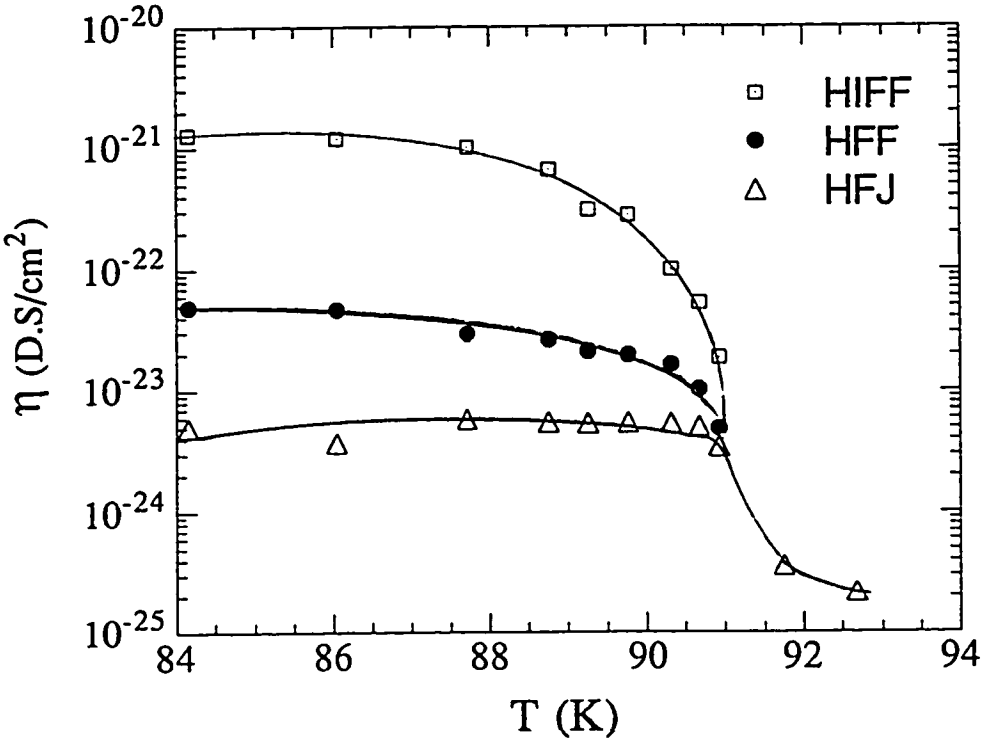

Figure 5.10: A semi-log plot of η vs. temperature for different regions for pure Y_{123}.

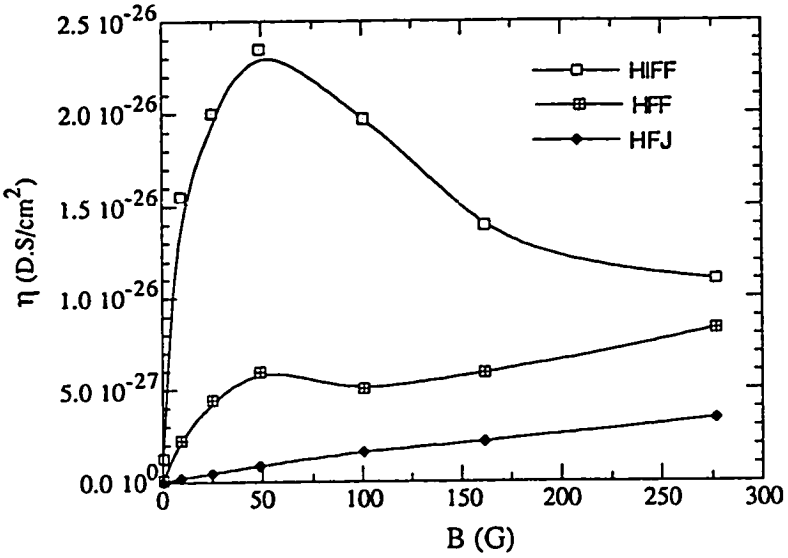

Figure 5.11: Viscosity coeff. η vs. field at T=87.6 K in different regions.

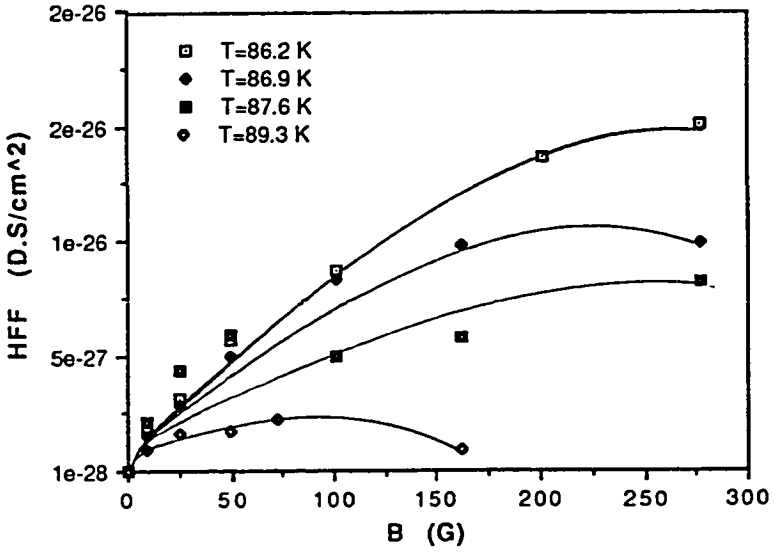

Figure 5.12: Viscosity coeff. HFF vs. field at different temperatures.

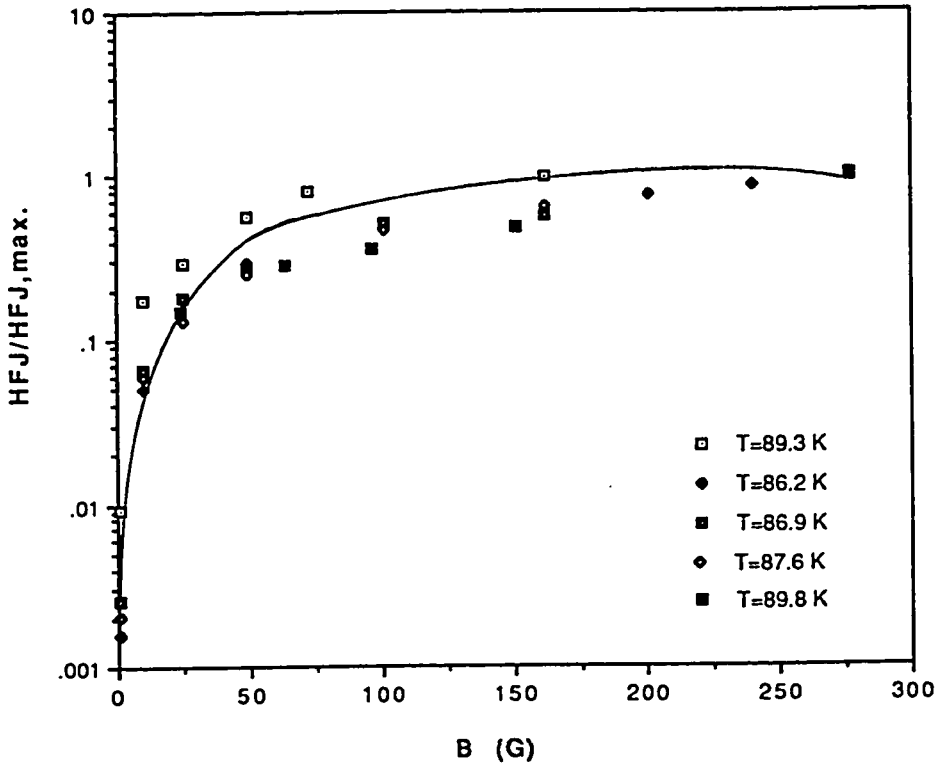

Figure 5.13: Normalized viscosity coeff. vs. field for different temperatures in the flux jump region.

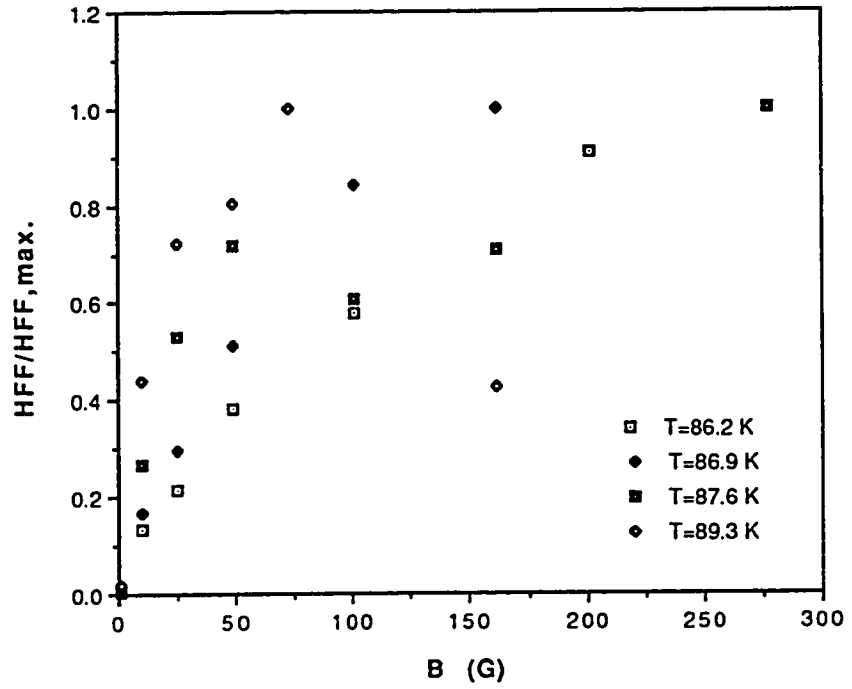

Figure 5.14: Normalized viscosity coeff. vs. field for different temperatures in the flux flow region.

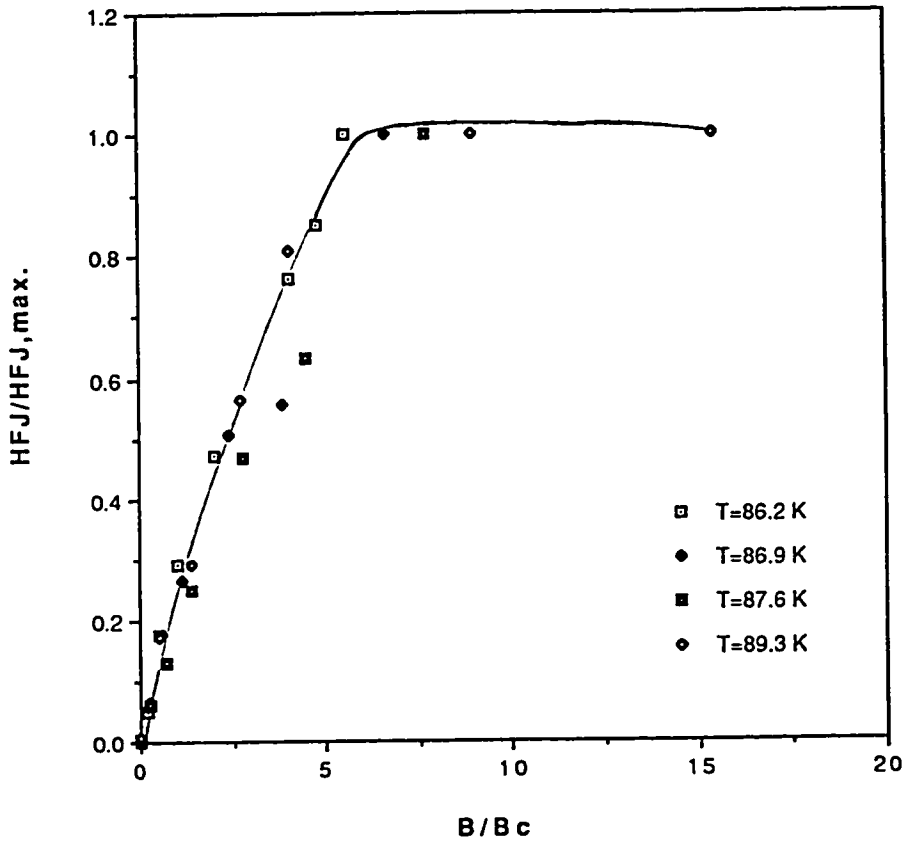

Figure 5.15: Normalized viscosity coeff. vs. normalized field (B/B_c) for different temperatures in the flux jump region.

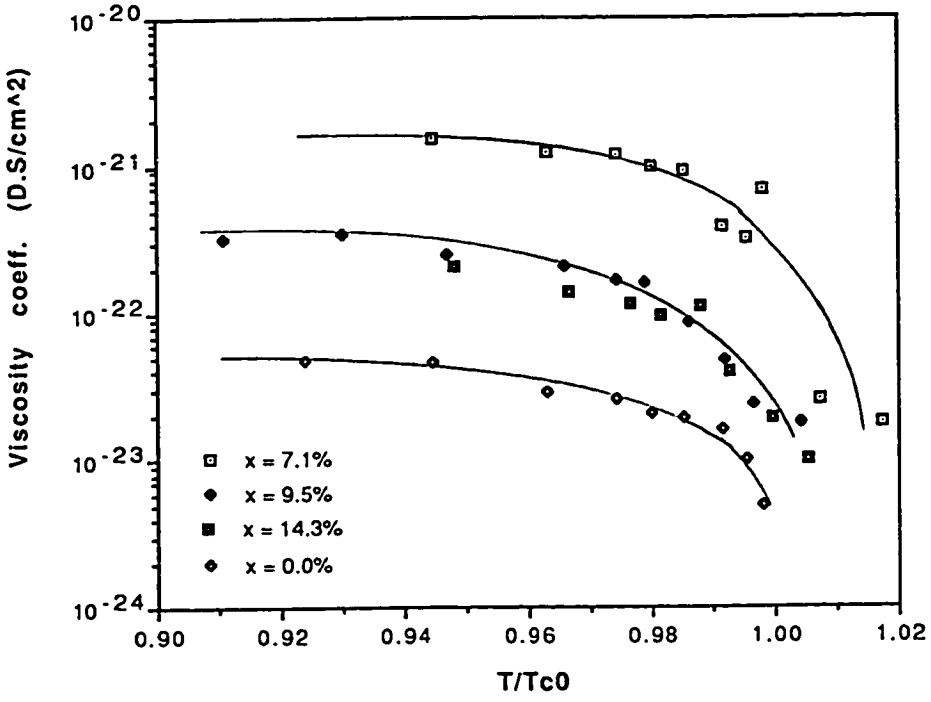

Figure 5.16: A semi-log plot of HFF vs. reduced temperature for different Ag_2O concentration x.

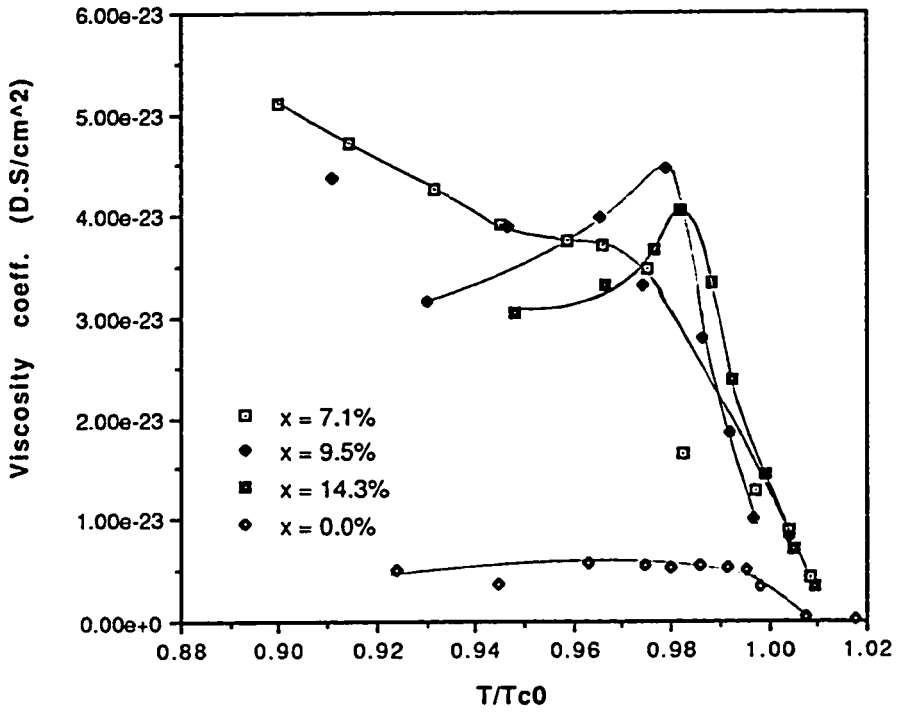

Figure 5.17: Viscosity coeff. (HFJ) vs. reduced temperature for different Ag_2O concentration x.

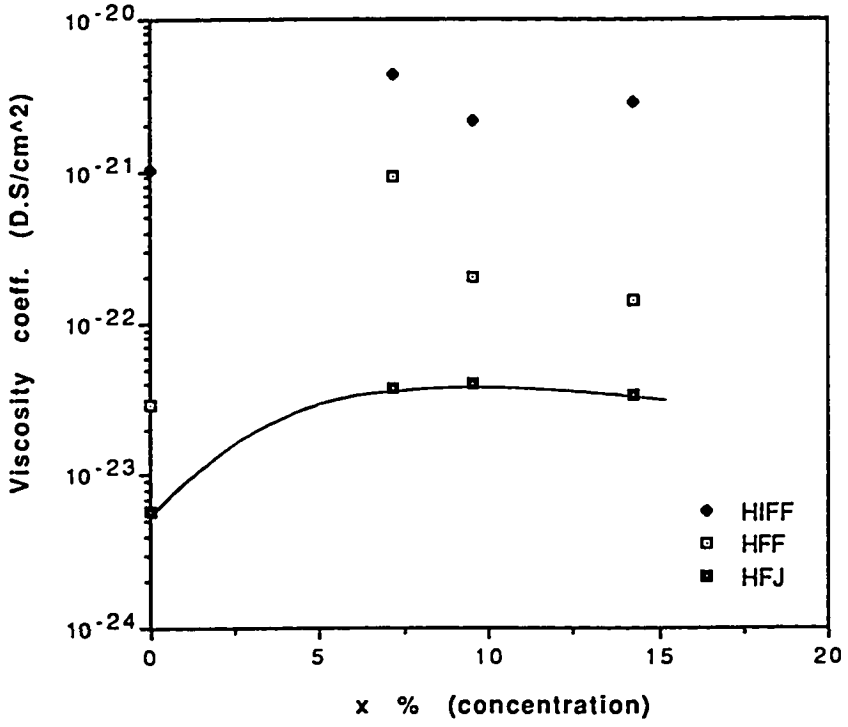

Figure 5.18: Viscosity coefficient vs. Ag_2O concentration x at temperature T=87.6 K in different regions.

Chapter 6

CONCLUSION

High quality samples of pure Y_{123} and $Y_{123}/(Ag_2O)_x$ composites have been prepared by the solid state reaction technique, and have been properly characterized using the resistivity measurements and X-Ray analysis. All prepared samples exhibit zero transition temperature in the range ($T_{c_0} = 90 - 92K$) and transition width in the range ($\Delta T = 1.1 - 1.6K$). Normal state resistance for all samples has been calculated, results indicated that addition of silver in $Y_{123}/(Ag_2O)_x$ composites reduces the normal state resistance and produces little changes in the transition temperature compared to pure Y_{123}. Our results are consistence with the available experimental results in this regard.

Critical currents and pinning forces have been studied using the (I-V)

technique. Near T_c critical currents for all samples exhibit a linear decreasing behaviour as a function of temperature, and a power law at lower temperature. The addition of silver enhances the critical currents for all silver concentration used (x=0-15 %, x=wt. ratios).

Critical currents measurements for different trapped flux states have been investigated. Results showed a rapid decrease in J_c for low cooling fields ($\sim B_{c_1}$), then a slow down occurs upon further increase in the field. Critical currents measurements have been used to obtain the critical fields (B_c and B_{c_2}) and pinning forces for different trapped flux states.

Pinning forces exhibit a scaling behaviour over the temperature and field ranges investigated. Scaling behaviour obtained is similar to that predicted by Fietz and Webb for conventional SC's.

Flux flow resistivity (in $Y_1$23) in all flux flow regions exhibits almost constant values at low temperature but upon approaching transition temperature it starts increasing rapidly reaching the normal state resistance.

Flux flow resistivity versus cooling field showed a minimum at low fields ($\sim B_c$) in all flux flow regions except in the intermediate region. For conventional SC's the minimum occurs at very high fields ($\sim B_{c_2}$),

which indicates a pronounced difference between the two classes of SC's.

Viscous flux motion has also been studied, viscosity coefficient η was obtained using the flux flow resistance and Kim's model. The general behaviour of η in all regions is almost the same, it exhibits a broad maximum at low temperature, then decreases rapidly near T_c. Maximum damping effects (maximum in η) occurs in the intermediate flux flow region and minimum in the flux jump region. In the later case, vortices move with higher velocity and so their motion is opposed with a relatively smaller viscous force. Viscosity coefficient η versus cooling field also exhibits a broad maximum at low fields ($\sim B_c$) near T_c, the peaks get sharper at higher temperature and their positions shifted towards lower fields.

For the $Y_{123}/(Ag_2O)_x$ composites, the flux flow resistivity in all regions has been studied. Our results indicate that flux flow resistivity decreases with increasing Ag_2O concentration, whereas for conventional SC's Kim et al. have showed experimentally, that addition of impurities produces no effect on the flux flow resistance.

Viscosity coefficient η versus temperature exhibits a sharp peaks below T_c for different Ag_2O concentrations, while for pure Y_{123} no such peaks have been observed. Our results in this regard agree with Clem's model

applied for conventional SC. Clem has showed that for an impure SC, η versus temperature shows a broad maximum whereas for sufficiently pure SC no peak effect can be seen.

Finally, we noticed that viscosity coefficient (η versus field) in the flux jump region shows a scaling behaviour as a function of the reduced field variable B/B_c, no scaling effects has been observed with reduced field B/B_{c_2}.

Bibliography

[1] Warner Buckel, **Superconductivity Fundamentals and applications**, VCH Verlagsgesellschaft Weinheim (Federal Republic of Germany) (1991).

[2] W. Meissner and R. Ochsenfeld, *Naturwissenschaften*, 21, 787 (1933).

[3] F. London and H. London, *Physica 2*, 341 (1935).

[4] A. B. Pippard, *Proc. Roy. Soc. London Ser.* A216, 547 (1953), and *Proc. Camb. Phil. Soc.* 47, 617 (1951).

[5] A. C. Rose-Innes and E. H. Rhoderick, **Introduction to Superconductivity**, Pergamon Press Ltd., Oxford 2nd Edtion (1978).

[6] V.L. Ginzburg and L.D. Landau, *Zh. Eksper. teor. Fiz.*, 20, 1064 (1950).

[7] M. Tinkham, **Introduction to Superconductivity**, McGraw-Hill, New York (1975).

[8] A. A. Abrikosov, *Zh. Eksper. teor. Fiz.*, 32, 1442 (1957).

[9] J. W. Lynn, **High Temperature Superconductivity**, Springer Verlag, New York (1990).

[10] R. D. Huebener, **Magnetic Flux Structure in Superconductors**, Springer-Verlg Berlin Heidelberg, New York (1979).

[11] J. Bardeen, L.N. Cooper, and J.R. Schrieffer, *Phys. Rev.* 108, 1175 (1957).

[12] J. G. Bednorz and K. A. Müler, *Z. Physik B*, 64, 189 (1986).

[13] Vladimir Z. Kresin, Stuart A. Wolf, **Fundamentals of Superconductivity**, Plenum Press, New York (1990).

[14] C. Kittel, **Introduction to Solid State Physics**, John Wiley, New York (1986).

[15] M. K. Wn, J. R. Ashburn, C. J. Torng et al., *Phys. Rev. Lett.*, 58, 908 (1987).

[16] Charles P. Poole, Jr., Timir Datta, and Horacio A., **Copper Oxide Superconductors**, John Wiley & Sons (1988).

[17] S. M. Fine, M. Greenblatt, S. Simizu and S. A. Friedberg, *Phys. Rev. B* 36, 5716 (1987).

[18] L. Ganapathi, Ashok Kumar and J. Narayan, *Mat. Res. Soc.* (MRS), Symp. Proc., Vol. 169, 1267 (1990).

[19] T. Penny, S. von Molnar, D. Kaiser, et. al., *Phys. Rev.B* 38, 2918 (1988).

[20] H. L. Stormer, A. F. J. Levi, K. W. Baldwin et. al., *Phys. Rev. B*, 38, 2472 (1988).

[21] Y. Shapira, C. V. Huang et. al., *Journal of Magnetism and Magnetic Materials* 78, 19 (1989).

[22] E. Holguin, J. F. Londe, H. Berger; *Physica C*, 197, 167 (1992).

[23] L. Ryelandt, M. Cassart, F. Delannay et. al., *Mat. Res. Soc.* (MRS) Symp. Proc., Vol 169, 1243 (1990).

[24] M. A. Ocampo, E. Orgaz, T. Akachi, *Mat. Res. Soc.* (MRS) Symp. Proc., Vol. 169, 1263 (1990).

[25] C. W. Chu, J. Bechtold, L. Gao et al.,*Phys. Rev. Lett.*, 60, 941 (1988).

[26] Thomas R. A. Skew, Richard B. Flippen, *Mat. Res. Soc.* (MRS) Symp. Proc., Vol 169, 939 (1990).

[27] L. W. Song, Y. H. Kao, Q. Y. Ying et al., *Mat. Res. Soc.* (MRS) Symp. Proc. Vol 169, 891 (1990).

[28] Th. Schuster, M. R. Kohlischka, T. Reininger et al., *Supercond. Sci. Technol.*, 5, 614 (1992).

[29] M. A. Beno, L. Soderholm, D. W. Capone et al., *Appl. Phys. Lett.*, 51, 57 (1987).

[30] C.P. Bean, *Phys. Rev. Lett.* 8, 250 (1962).

[31] S. Senoussi, *Journal de Physique III*, July or August (1992).

[32] M. Nikolo, R.B. Goldfarb, *Phys. Rev. B* 339, 6615, (1988).

[33] N. Hamdan, K. Ziq, *Workshop on Materials and Material Sciences*, Sultan Qabous University, Jan 18-29, (1992).

[34] H. Kumakura, M. Uchara et. al., *Phys. Lett A* 124, 367 (1987).

[35] Edward J. Kramer, *J. Appl. Phys.*, 44, 1360 (1973).

[36] M. E. Reeves, B. D. Weaver, D. A. Krieger et al., *Phys. Rev. B*, 45, 4585 (1992).

[37] J. Y. Juang, S. J. Wang et al., *Phys. Rev. B*, 46, 1188 (1992).

[38] C. D. Wei, Z. X. Liu, Z. Z. Gan, *Physica C*, 195, 286 (1992).

[39] L. W. Song, M. Yang et al., *Phys. Rev. B*, 45, 3083 (1992).

[40] W. A. Fietz and W. W. Webb, *Phys. Rev.*, 178, 657 (1969).

[41] Y. B. Kim, C. F. Hempstead, and A. R. Strnad, *Phys. Rev.*, 139, A1163 (1965).

[42] P. W. Anderson, *Phys. Rev. Lett.*, 9, 309 (1962).

[43] P. W. Anderson, and Y. B. Kim, *Rev. Mod. Phys.*, 36, 39 (1962).

[44] M. Tinkham, *Mat. Res. Soc.* (MRS), Symp. Proc., Vol. 169, 1849 (1990).

[45] John R. Clem, *Phys. Rev. Lett.*, 20, 735 (1968).

[46] E. A. Lynton, **Superconductivity**, Science Paperbacks by Champem and Hall Ltd. London (1971).

[47] W. Desorbo, *Rev. Mod. Phys.*, 36, 90 (1964).

[48] E. S. Rosenblim, S. H. Autler, and K. H. Gooen, *Rev. Mod. Phys.*, 36, 77 (1964).

NOMENCLATURE

α	temperature coefficient
B_c	thermodynamic critical magnetic field
B_{c_1}	lower critical field of type-II superconductors
B_{c_2}	upper critical field of type-II superconductors
I	current
ΔT	transition width
η	viscosity coefficient
FC	field cooled
FFR	flux flow resistance
FJR	flux jump resistance
F_L	Lorentz force
F_P	pinning forces per unit volume
g_n	Gibbs free energy per unit volume of normal phase
g_s	Gibbs free energy per unit volume of superconducting phase
G_n	Gibbs free energy of specimen in normal phase
G_s	Gibbs free energy of specimen in superconducting phase
HFF	viscosity coefficient in the flux flow region
HFJ	viscosity coefficient in the flux jump region
HIFF	viscosity coefficient in the intermediate flux flow region
Hi-T_c	high transition temperature

IFFR	intermediate flux flow resistance
(I-V)	current-voltage characteristics
J_c	critical current density
J_{c_1}	lower (intergrain) critical current density
J_{c_2}	upper (intragrain) critical current density
J_{gb}	grain boundary critical current density
κ	Ginzburg-Landau parameter
λ_L	penetration depth
LHe	liquid helium
LN_2	liquid nitrogen
n_s	superelectrons density
ρ_f	flux flow resistivity
ρ_n	normal state resistivity
T_c	transition (critical) temperature
T_{c0}	zero transition temperature
SC	superconductor
x	concentration of silver-oxide (Ag_2O)
ξ	coherence length
XRD	X-Ray diffraction
Y_{123}	$Y_1Ba_2Cu_3O_{7-\delta}$
ZFC	zero field cooled